UNIVERSITY OF CALIFORNIA,
IRVINE

# Roll-to-Roll, Shrink-Induced Superhydrophobic Surfaces for Antibacterial Applications, Enhanced Point-of-Care Detection, and Blood Anticoagulation

DISSERTATION

submitted in partial satisfaction of the requirements
for the degree of

DOCTOR OF PHILOSOPHY

in Biomedical Engineering

by

Jolie McLane Nokes

Dissertation Committee:
Associate Professor Michelle Khine, Chair
Professor Abraham Phillip Lee
Associate Professor Elliot Hui

2015

# DEDICATION

To

my parents Fred and Kathy McLane

my siblings Eric, Mark, and Kristen McLane

my husband Riley Nokes

my dogs Rocky and Lucy Nokes

# TABLE OF CONTENTS

# LIST OF FIGURES

# LIST OF TABLES

# ACKNOWLEDGMENTS

I would like to express my appreciation to my academic advisor Dr. Michelle Khine. She has been an inspiration and role model throughout my academic career, and words cannot express how truly grateful I am to have her as my adviser. She has guided me through my experiments, challenged me to invent innovative products, and inspired me to go above and beyond my expectations. Even further, I know that she genuinely cares about her students, and I appreciate all she has done for me. She is the most passionate person I have met, and I am honored to be a part of her lab family.

Also thank you to my defense and qualifying committee members: Dr. Abraham Lee, Dr. Elliot Hui, Dr. Ali Morhaz, and Dr. Edwin Monuki. They have given me foresight and productive critiques to my project, and I thank them for challenging me.

I would like to thank all collaborations with schools and companies. I have collaborated with VTT Technical Research Centre of Finland to scale-up manufacturing of my technology, which has been an integral part of my PhD thesis. Companies have been interested in my surfaces, and I would like to thank them for working with me as I have been scaling up my samples and performing experiments.

My lab members have been integral to my dissertation, and I would like to thank Ralph Liedert, Chun Wu, Ali Siddiqui, Lauren Freschauf, Dr. Himanshu Sharma, Sophia Lin, Jon Pegan, Dr. Aaron Chen, Eugene Lee, Scott Strayer, Jay Lepere, Michael Chu, and all Khine Lab members. I would also like to thank the many friends I have made throughout graduate school such as Dr. Monica Kim and Dr. Arlene Doria Martin. Everyone has been like a second family to me and has significantly improved my PhD experience. I thank them for helping me with experiments and especially thank them for helping me through the hardships of graduate school.

Thank you to my family for supporting me since I was a child. My parents have always inspired me to do great things and instilled a fundamental desire to be the best I can be. They unknowingly taught me to be an engineer even as a young child – by letting me "work on the car" with my Daddy (i.e. hold the flashlight and constantly ask "what's that?") and crunch numbers with my Mom every day. They always pushed me to pursue my dreams and continually gave me love and support. My siblings have always been my best friends and have supported me through my academic career, helping me with life and academic hardships. I am so thankful to have such a wonderful and loving family, and words cannot express how grateful I am to have them in my life.

Finally, I would like to thank my loving husband Riley Nokes. His love and support are endless, and he's helped me succeed in graduate school as well as in life. His love inspires me to constantly challenge myself and become a better person. He has supported and helped me with the final push to the finish line, and I cannot thank him enough. I look forward to our wonderful future together, and I know he will make a great partner to push me further than I ever thought possible.

I am blessed to have so many amazing and inspirational people in my life. Thank you to everyone who has helped me throughout graduate school. I am so fortunate to have a support team helping me succeed, and I owe all my success to the people in my life. Thank you!

# CURRICULUM VITAE

**JOLE MCLANE NOKES**

EDUCATION

2015 Ph.D. in Biomedical Engineering, University of California, Irvine
Thesis: *"Roll-to-Roll, Shrink-Induced Superhydrophobic Surfaces for Antibacterial Applications, Enhanced Point-of-Care Detection, and Blood Anticoagulation"*

2012 M.S. in Biomedical Engineering, University of California, Irvine
Thesis: "*Shrink-Induced Patterned Superhydrophobic Plastics for Point-of-Care*"

2010 B.S. in Bioengineering, University of California, Merced

PUBLICATIONS

1) Nokes J.M., Liedert R., Kim M., Siddiqui A., Chu M., Lee E., Khine M. (submitted 2015). Reduced Blood Coagulation on Roll-to-Roll, Shrink-Induced Superhydrophobic Plastics, Advanced Healthcare Materials.
2) McLane J., Wu C., Khine M. (2015). Enhanced Detection of Protein in Urine on a Superhydrophobic Plastic, Advanced Functional Materials, 2: 1.
3) Nawarathna, D., Norouzi, N., McLane, J., Sharma, H., Sharac, N., Grant, T., Chen, A., Strayer, S., Ragan, R., and Khine, M (2013). Shrink-induced sorting using integrated nanoscale magnetic traps, Applied Physics Letters, 102: 063504.
4) Jayadev, S., Pegan, J., Dyer, D., McLane, J., Lim, J., Khine, M. (2012). Adaptive wettability-enhanced surfaces ordered on molded etched substrates using shrink film, Smart Materials and Structures, 22: 014014.
5) Freschauf L.R.,* McLane J.,* Sharma H., Khine M. (2012) Shrink-induced superhydrophobic and antibacterial surfaces in consumer plastics, PLoS ONE 7: 8.
6) Nguyen, D., McLane, J., Lew, V., Pegan, J., and Khine, M. (2011). Shrink-film microfluidic education modules: Complete devices within minutes, Biomicrofluidics, 5: 022209.

INTELLECTUAL PROPERTY

1) Khine, M., McLane J., Lin, E., Lin, S. A Hundred Tiny Hands. Submitted copyright 2015 Mar 16.
2) Khine, M., McLane J., Liedert, R. Scalable Manufacturing of Superhydrophobic Structures in Plastics. Patent filed 2014 December 9.
3) Khine, M., McLane, J., Wu, C. Shrink-Induced Self-driven Microfluidic Devices and Evaporation on Superhydrophobic Surfaces for Detection Using Bodily Fluids. Submitted patent 2014 August 29.
4) Khine, M., McLane, J., Mendoza, N. Superhydrophobic Induced High Numerical Aperture Plastic Lenses. US patent 20150094219 A1. 2013 Sep 20.
5) Khine, M., Freschauf, L., McLane, J. Shrink-Induced Antimicrobial Surfaces in Consumer Plastics. US patent 20130309450 A1. 2013 May 9.
6) Khine, M., Sharma, H., Lin, S., McLane, J. Rapid Inexpensive Fluoroimmunoassay Diagnostic Chip Fabricated from Polyolefin Coated with a Thin Film. US patent 20120202702 A1. 2012 Feb 6.

PRESENTATIONS

1) Presentation, "Reduced Blood Coagulation on Roll-to-Roll, Shrink-Induced Superhydrophobic Plastics," *SoCal Micro and Nanofluidics Symposium*, Regional Meeting, Pasadena, CA, June 2015.
2) Poster, "Roll-to-Roll Shrink-Induced Superhydrophobic Surfaces for Enhanced Point-of-Care Detection in Urine," *Center for Advanced Design and Manufacturing of Integrated Microfluidics (CADMIM)*, International Meeting, Irvine, CA, March 2015.
3) Poster, "Roll-to-Roll Shrink-Induced Superhydrophobic Surfaces for Enhanced Point-of-Care Detection in Urine," *IEEE-EMBS Micro and Nanotechnolgoy in Medicine Conference (MNMC)*, International Conference, Kahuku, HI, December 2014.
4) Poster, "Shrink-Induced Superhydrophobic Surfaces for Enhanced Detection, Microfluidics, and Educational Outreach," *UC Symposium*, Regional Conference, Irvine, CA, June 2014.
5) Poster, "Shrink-Induced Superhydrophobic Surfaces for Enhanced Detection, Microfluidics, and Educational Outreach," *IEEE-EMBS Graduate Student Industry Night*, Regional Event, Irvine, CA, April 2014.
6) Poster, "Shrink-Induced Superhydrophobic Surfaces for Enhanced Detection, Microfluidics, and Education Outreach," Center for Advanced Design and Manufacturing of Integrated Microfluidics (CADMIM), International Meeting, Irvine, CA, April 2014.
7) Poster, "Shrink-Induced Superhydrophobic Microfluidics for Enhanced Detection," *Gordon Research Conference/Seminar*, International Conference, Barga, Italy, June 2013.
8) Poster, "Shrink-Induced Superhydrophobic Microfluidics," *IEEE-EMBS Graduate Student Industry Night*, Regional Event, Irvine, CA, April 2013.
9) Poster, "Shrink-Induced Superhydrophobic Microfluidics," *IEEE-EMBS Micro and Nanotechnolgoy in Medicine Conference (MNMC)*, International Conference, Ka'anapali, HI, December 2012.
10) Poster, "Shrink-Induced Superhydrophobic Microfluidics," *DARPA Meeting*, National Conference, Irvine, CA, August 2012.
11) Poster, "Shrink-Induced Superhydrophobic Microfluidics," *UC Symposium*, Regional Conference, Berkeley, CA, June 2012.
12) Poster, "Shrink-Induced Superhydrophobic Surfaces," *LifeChips Conference*, Regional Conference, Irvine, CA, February 2012.
13) Poster, "Shrink-Induced Superhydrophobic Surfaces," *Micro Total Analysis Systems (μTAS)*, International Conference, Seattle, WA, October 2011.
14) Poster, "Shrink-Induced Superhydrophobic Surfaces," *Technologies for Future Micro-Nano Manufacturing (MFG*), National Conference, Napa Valley, CA, August 2011.
15) Poster, "Shrink-Induced Superhydrophobic Surfaces," *Micro/Nano Fluidics Fundamentals Focus (MF3) Meeting*, International Conference, Irvine, CA, May 2011.

HONORS AND AWARDS

1) National Science Foundation Industry/University Cooperative Research Center (NSF I/UCRC), "Micro Superhydrophobic Ultra Rapid Fluidics (MicroSURF)", Fundamental Research Program (FRP) grant, July 2015-July 2017
2) Poster Award at Institute of Electrical and Electronics Engineers-Engineering in Medicine and Biology Society (IEEE-EMBS) Micro and Nanotechnolgoy in Medicine Conference (MNMC), International Conference presenter, December 2014
3) National Institute of Health (NIH) Supplement to Promote Diversity in Health Research Fellowship (PA-12-149), Research Fellow, August 2013-June 2015
4) National Science Foundation Integrative Graduate Education and Research Traineeship (NSF-IGERT) LifeChips Graduate Student Research Fellowship, Research Fellow, July 2010-July 2013

# ABSTRACT OF THE DISSERTATION

Roll-to-Roll, Shrink-Induced Superhydrophobic Surfaces for Antibacterial Applications, Enhanced Point-of-Care Detection, and Reduced Blood Coagulation

By

Jolie McLane Nokes

Doctor of Philosophy in Biomedical Engineering

University of California, Irvine, 2015

Professor Michelle Khine, Chair

Superhydrophobic (SH) surfaces are desirable because of their unique anti-wetting behavior. Fluid prefers to bead up (contact angle >150˚) and roll off (contact angle hysteresis <10˚) a SH surface because micro- and nanostructure features trap air pockets. Fluid only adheres to the peaks of the structures, causing minimal adhesion to the surface. Here, shrink-induced SH plastics are fabricated for a plethora of applications, including antibacterial applications, enhanced point-of-care (POC) detection, and reduced blood coagulation. Additionally, these purely structural SH surfaces are achieved in a roll-to-roll (R2R) platform for scalable manufacturing.

Because their self-cleaning and water resistant properties, structurally modified SH surfaces prohibit bacterial growth and obviate bacterial chemical resistance. Antibacterial properties are demonstrated in a variety of SH plastics by preventing gram-negative *Escherichia coli* (*E. coli*) bacterial growth >150x compared to flat when fluid is rinsed and >20x without rinsing. Therefore, a robust and stable means to prevent bacteria growth is possible.

Next, protein in urine is detected using a simple colorimetric output by evaporating droplets on a SH surface. Contrary to evaporation on a flat surface, evaporation on a SH surface allows

fluid to dramatically concentrate because the weak adhesion constantly decreases the footprint area. On a SH surface, molecules in solution are confined to a footprint area 8.5x smaller than the original. By concentrating molecules, greater than 160x improvements in detection sensitivity are achieved compared to controls. Utility is demonstrated by detecting protein in urine in the pre-eclampsia range (150-300$\mu gmL^{-1}$) for pregnant women.

Further, SH surfaces repel bodily fluids including blood, urine, and saliva. Importantly, the surfaces minimize blood adhesion, leading to reduced blood coagulation without the need for anticoagulants. SH surfaces have >4200x and >28x reduction of blood residue area and volume compared to the non-structured controls of the same material. In addition, blood clotting area is reduced >5x using whole blood directly from the patient.

In this study, biocompatible SH surfaces are achieved using commodity shrink-wrap film and are scaled up for R2R manufacturing. The purely structural modification negates complex and expensive post processing, and SH features are achieved in commercially-available and FDA-approved plastics.

# CHAPTER 1: INTRODUCTION

## 1.1 Motivation

### *1.1.1 Commercial Applications of Plastics*

Plastics are used for a wide variety of applications, ranging from everyday consumer products to complex medical instruments. The Federal Drug Administration (FDA) deems plastics such as polypropylene (PP), polyethylene (PE), and polystyrene (PS) safe for food and medical use[1] and therefore, such plastics are used extensively. Often, plastics are not directly compatible for medical applications and must undergo processing to be functional. For example, external and implantable polymers cause adverse effects such as blood thrombosis, septicemia, hemolysis, and protein adsorption.[2,3] To combat these side effects, polymers are coated with chemicals that decrease or diminish the adverse responses.[2–4] Alternatively, patients can be treated with medication to combat side effects, such as anticoagulant chemicals to prevent thrombosis.[3]

Chemical coatings and medications can have drawbacks,[5] however, and there is a need for a biocompatible material that will not adversely affect patient health. In addition, the material must be easily employed with current plastic manufacturing techniques. Rather than chemically modifying a plastic, structural modification is desirable to alter the characteristics of a plastic. Structurally modified polymers have been shown to affect thrombosis,[2] bacterial adhesion,[6] fluid behavior,[7–9] and diagnostics.[7,10] By controlling the interaction between the structured polymer and bodily fluids, a structurally modified polymer can behave similarly to coatings and medications without the adverse drawbacks. Further, purely structural modification negates excess processing steps for manufacturing, and modifications can be achieved directly in the plastic.

### *1.1.2 Biomimetic Inspiration*

Structurally modified substrates are seen in nature, and organisms leverage the altered properties of structural modification for various applications. For example, the lotus leaf is known for its self-cleaning and superhydrophobic (SH) properties due to its micro and nanoscale roughened papillae.[11] Similarly, rose petals, butterfly wings, springtails, termite wings, desert beetles, water striders, and many more organisms leverage micro and nanoscale features to achieve superhydrophobicity[11–19] for self-cleaning, bacterial resistance, flight efficiency, water retention and removal, heating and cooling, and water travel.[11,20,21] In addition to the structural modification, these plants and animals have chemical coatings that lower the surface energy and prevent water from wetting the surface.[8,22,23]

### *1.1.3 Superhydrophobic Biomaterial Applications*

The self-cleaning, non-wetting, anti-fouling, antibacterial, low adhesion, and anticoagulant nature of SH surfaces begs the need for commercial products with these characteristics. Such characteristics could benefit medical tubing, catheters, food packaging, biosensors, films and coatings, and many more. In addition, the ease of manufacturing purely structured SH surfaces would allow easy access of these commercial products to consumers.

## 1.2 Overview of the Dissertation

### *1.2.1 Superhydrophobic Surfaces*

Chapter 2 focuses on superhydrophobic (SH) surfaces, the theory of superhydrophobicity, and the fundamental fabrication of shrink-induced SH surfaces. Briefly, SH surface are desirable because of water's unique interaction with the surfaces. Water does not wet SH surfaces but rather beads

up and slides off the surface. SH surfaces have micro- to nanoscale features with peaks and valleys that trap air. Water only contacts the peaks of the hierarchical structures and has minimal adhesion with the surface. This behavior allows SH surfaces to be non-wetting and self-cleaning, giving rise to many commercial applications.

Here, SH surfaces are achieved by depositing a thin bilayer of metal on the pre-stressed polymer polyolefin (PO). PO shrink 20x in area when heat is applied, and the thin, stiff layer of metal on the surface causes the substrate to form wrinkles during the shrinking process. These wrinkle features are micro- to nanoscale and trap pockets of air when fluid is applied to the surface, thus achieving superhydrophobicity. These SH features can subsequently be imprinted into inherently hydrophobic materials, such as silicones and plastics, to exponentially achieve SH products.

### *1.2.2 Scale-Up Manufacturing*

Chapter 3 focuses on the scale-up manufacturing of the SH surfaces. Initially, the SH surfaces were small silicone samples about the size of a quarter. Next, the SH features were imprinted into hard plastics, making the samples more desirable for commercial applications. Finally, we have worked with VTT Technical Research Centre of Finland to scale up manufacturing of the SH surfaces in a roll-to-roll (R2R) platform. Figure 1.1 shows an evolution of the SH samples construction. The samples shown are bigger than a hand (~10cm in width) and can be extended any length. The SH features can also be imprinted into a variety of hard plastics for commercial use.

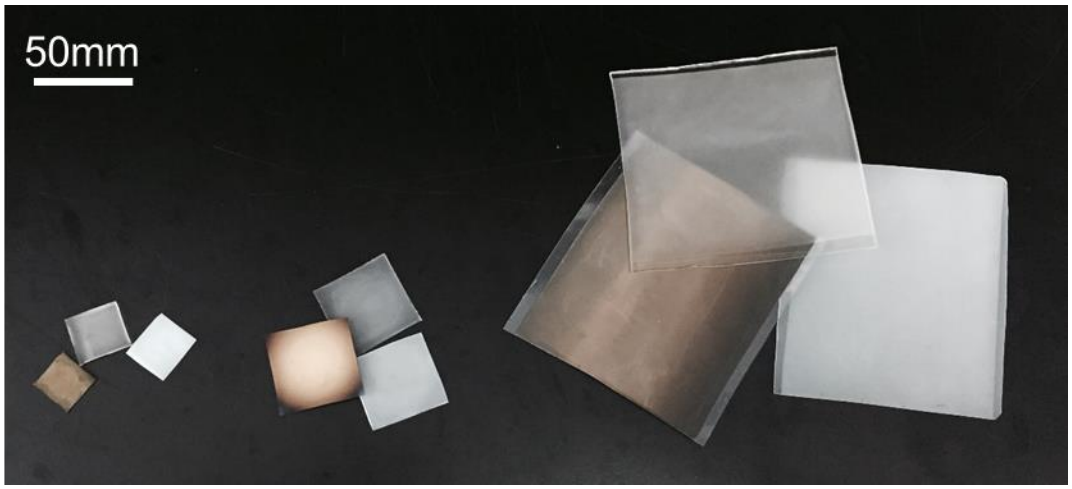


**Figure 1.1**: Superhydrophobic surfaces were initially small silicone samples and have evolved into large areas of plastic using roll-to-roll manufacturing.

### *1.2.3 Applications of Superhydrophobic Surfaces*

Amongst other applications, SH surfaces are desirable because they are antibacterial (Chapter 4), can be used for enhanced point-of-care diagnostics (Chapter 5), and reduce blood coagulation (Chapter 6).

Because of the low surface energy of the SH surfaces, bacteria cannot adhere and grow on the surfaces. *Escherichia coli* (*E. coli*) is placed on flat and SH surfaces, and SH surfaces reduce bacterial adhesion >20x compared to flat surfaces. In addition, due to the self-cleaning nature of the SH surfaces, rinsing the SH surfaces decreased bacterial adhesion >150x compared to flat. Overall, total bacteria adhesion is reduced >1500x on the SH surfaces and >10x on the flat surfaces.

SH surfaces are also used to enhance protein detection in urine. By simply evaporating droplets with low concentration on a SH surface, molecules are highly concentrated to a small pellet (8.5x smaller than the initial footprint and infinitely smaller than the initial volume). These pellets can undergo simple colorimetric assays to detect previously undetected concentrations of protein, and

we have seen >160x enhancements compared to controls. With this method, protein levels indicative of pre-eclampsia can detected and distinguished from normal levels of protein in urine.

Blood coagulation is reduced on the SH surfaces compared to flat. Upon adhering to a surface, platelet cells trigger the blood coagulation cascade to form a blood clot. Because SH surfaces have minimal adhesion, platelet cells are less activated on a SH surface compared to a flat surface. We have shown >4200x reduction in blood residual area and >28x reduction in blood residual volume on a SH surface. Additionally, blood coagulation has reduced >5x compared to flat, and platelet maturity and fibrin network formation are less advanced on the SH surfaces.

Chapter 7 focuses on further avenues of research with SH surfaces. The conformal nature of the commodity shrink film allows for 3-dimensional SH shapes. Thus, microfluidic applications can be achieved. In addition, the SH surfaces can be patterned for molecular capture, and a single device can be achieved to enhance disease detection.

# CHAPTER 2: Superhydrophobic Surfaces

## 2.1 Introduction of Superhydrophobicity

### *2.1.1 Superhydrophobic Surfaces*

On a superhydrophobic (SH) surface, water prefers to bead up and roll off the surface rather than wet the surface. Because surface tension is high at the solid-liquid interface of SH surfaces, water beads into a sphere to conserve energy.[8,15,20,22,24] SH surfaces have a contact angle (CA) greater than 150° and a sliding angle (SA) less than 10° with water. CA measures the water droplet angle at the solid-liquid interface, and SA measures the angle at which a water droplet will slide off the surface when tilted.[8,20,22,24] Figure 2.1 shows a diagram of CA measurements of a hydrophobic and hydrophilic surface.

### *2.1.2 Superhydrophobic Fabrication*

Superhydrophobicity can be achieved artificially through structural[25,26] or chemical[27,28] alterations to allow for free movement of water across a surface. Current fabrication techniques employ complex production methods such as photolithography,[29,30] chemical vapor deposition,[31] and self-assembled monolayers[32] to create highly organized structures. Heterogeneous micro- to nanoscale structures can also achieve superhydrophobicity, and common production techniques utilize gels, colloids, and oxides.[25,26,33,34] In addition, post processing with chemical additives (such as fluorocarbons and hydrocarbons) are required to achieve low surface energies indicative of superhydrophobicity.[35,36]

However, these fabrication methods pose technical challenges to manufacturing as well as time consuming and costly barriers to production. By simplifying the fabrication process to achieve scale-up manufacturing and structural integration into existing surfaces, the benefits of SH surfaces

can be readily available to a range of materials for various biomedical (e.g. implants, coatings) as well as for consumer applications.

## 2.2 Superhydrophobic Theory

### *2.2.1 Young's Theory*

The phenomenon of superhydrophobicity is explained in part by a triad of equations that thermodynamically balances the interaction of the solid, liquid, and vapor phases. The fluid drop shape created between water and a smooth, flat surface can be calculated using Young's equation[37] where the three interfaces, solid-vapor $\lambda_{SV}$, solid-liquid $\lambda_{SL}$, and liquid-vapor $\lambda_{LV}$, describe the material's resulting water CA $\theta_Y$ during thermodynamic equilibrium (1).

$$\lambda_{SV} - \lambda_{SL} - \lambda_{LV} \cos\theta_Y = 0 \tag{1}$$

In particular, as the solid-liquid interfacial tension increases, the droplet's CA increases, and there is less surface contact between the droplet and the surface.[38] Figure 2.2a shows the CA resulting from the interfacial surface tensions on a smooth surface.

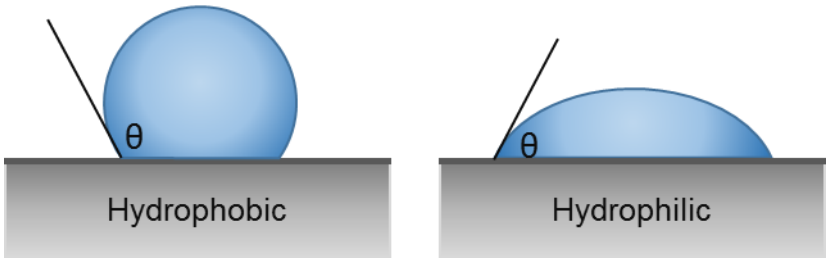


**Figure 2.1**: CA of a hydrophobic and hydrophilic surface. Water prefers to bead up on a hydrophobic surface and has a high CA θ. Water prefers to spread out on the hydrophilic surface and has a low CA θ.

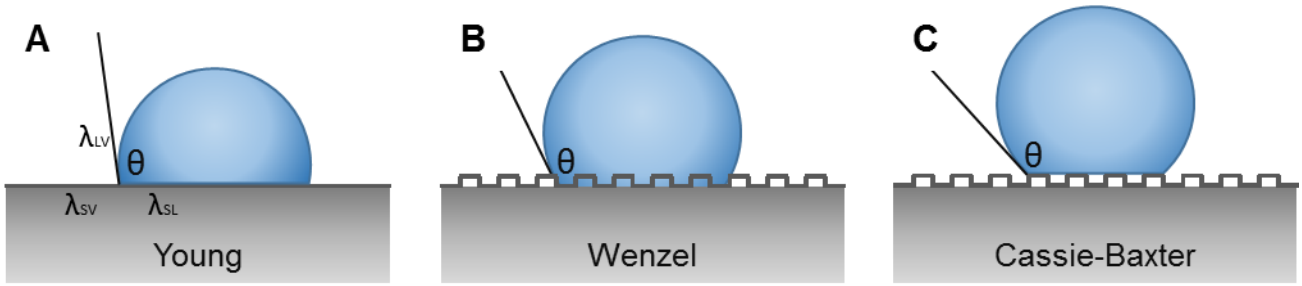


**Figure 2.2**: Theories of wetting. (A) Young's equation predicts the behavior of water on a smooth surface. (B) Water follows Wenzel's equation when the surface is roughened, and the CA is increased. (C) Air trapped in multiscale features prevents water from wetting the entire surface in the Cassie-Baxter theory, and the CA is further increased.[19]

### *2.2.2 Wenzel's Theory*

Further analysis of wetting can be performed with Wenzel's theory[9] where the roughness factor $r$, determined by a ratio of the geometric surface to the apparent surface, is directly associated with the change in CA $\theta_W$ of the roughened surface (2), as shown in Figure 2.2b.

$$\cos\theta_W = r\cos\theta_Y \tag{2}$$

As the surface is roughened, the contact area between the droplet and the surface is enhanced. If the solid-liquid surface tension is initially strong, the CA will increase due to increased contact between the droplet and surface. In more general terms, this equation explains the ability to increase hydrophobicity on hydrophobic surfaces and increase hydrophilicity on hydrophilic surfaces merely through roughening the surface and increasing the solid-liquid interface.

### *2.2.3 Cassie-Baxter Theory*

Another model was developed by Cassie and Baxter[8] in which the surface roughness is enhanced so greatly that water only contacts the peaks of the roughened surface (Figure 2.2c). Air pockets are trapped in the valleys of the roughened surface so that the water droplet interacts with the solid as well as the vapor phase at the apparent surface. This increase in liquid-vapor contact further enhances the CA of the water droplet. The summation of interactions between the liquid with the

solid and vapor determines the CA $\theta_C$ and is characterized by the Cassie-Baxter equation (3), where $\Phi$ is the solid fraction of the droplet in direct contact with the solid surface.

$$\cos\theta_C = \Phi\cos\theta_Y + \Phi - 1 \quad (3)$$

The high surface tension, minimal surface contact, and ease of movement exhibited by water on SH surfaces can be attributed to the presence of multiscale (micro- to nanoscale) structures.[20] Cheng et al. demonstrated the importance of these features on the lotus leaf by removing the nanostructures which resulted in a decrease in water contact angle, as predicted.[11] Furthermore, surfaces must be inherently hydrophobic[9] and have a low surface energy[39] to become superhydrophobic when structurally modified.

## 2.3 Superhydrophobic Features

### *2.3.1 Wrinkling Phenomenon*

Wrinkles are generated by mechanical instabilities of soft matter.[40,41] A thin film of a stiff material with a relatively higher Young's modulus can be deposited on the surface of a thicker, relatively soft substrate to create a bilayer system. By applying a compressive force to the bilayer system, the mismatch in stiffness causes the thin, stiff film to buckle and generate wrinkles, as shown in Figure 2.3. The wavelength of wrinkles can be controlled by the thickness of the stiffer material as well as the Young's moduli of the thin material and soft substrate. The amplitude of the wrinkles can be controlled by the film thickness as well as the amount of strain and critical strain of the bilayer system.[40,41]

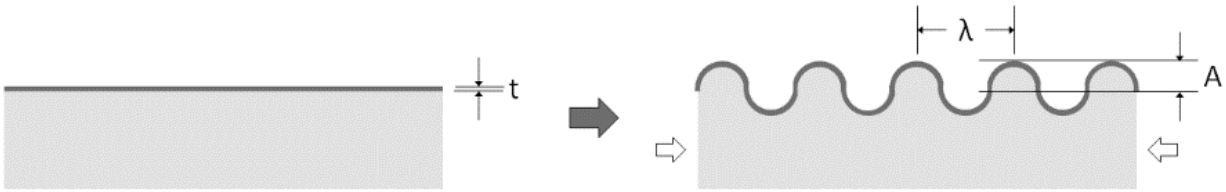


**Figure 2.3**: Wrinkles are created by compressing a bilayer with a mismatch in stiffness. The wavelength and amplitude of wrinkles can be controlled by the thickness of the film, the Young's moduli of materials, and the strain of the bilayer.

Wrinkles can be seen in nature and have been artificially generated as biomimetic substrates.[42–46] Commonly, a polymer substrate (such as polydimethylsiloxane (PDMS)) is stretched, a thin film (such as an oxide) is deposited on the stretched polymer substrate to generate a stiff film, and upon release of the bilayer system, wrinkles are formed. Khare et al. has created tunable, open-channel microfluidic systems using anisotropic sinusoidal grooves formed by wrinkles from stretched PDMS and oxide, and the fluidic wetting behavior on the grooves has been characterized corresponding to the amount of bilayer compression. The Khine Lab leverages their pre-stressed shrink polymer to achieve wrinkles by depositing a thin bimetallic film on the polymer surface. Upon heat, the polymer shrinks, and micro- to nanoscale wrinkles are formed, as shown in Figure 2.4.[42,43] Uniaxial or biaxial wrinkles are achieved by compressing uniaxially or biaxially. Lee et al. has generated anisotropic hierarchical wrinkles in polymer films by compressing the bilayer system uniaxially. The wavelength and amplitude of wrinkles has been successfully controlled to yield tunable wrinkles.

Wrinkles have been used to modify fluid behavior on substrates due to the enhanced roughness, and SH surfaces have been created using wrinkles.[6,7,44,45] Rahmawan et al. achieves wrinkles by forming diamond-like carbon on PDMS. This mismatch in stiffness forms wrinkles, and the features are in the SH regime. Freschauf et al. utilizes the wrinkles formed from the mismatch in stiffness from their shrink substrate and bimetallic film to achieve SH features. These features can

be imprinted into various materials and are used for antibacterial applications. Manna et al. also leverages the shrink film with a cross-linked stiff film to achieve SH features in molded shapes.

### *2.3.2 Pre-stressed Polymer*

The Khine Lab leverages pre-stressed polymers as a platform for fabrication.[42,47–50] Polyolefin (PO) is a biaxially stretched thermoplastic that isotropically shrinks 20x in area when heated above its glass transition temperature (160°C). By patterning PO at the macroscale and shrinking, high resolution devices can be fabricated using inexpensive equipment, thereby minimizing costs of manufacturing. Because the shrink substrate is a plastic, it is compatible with commercial production such as roll-to-roll manufacturing and scale-up production. The PO can also withstand many harsh conditions associated with fabrication such as chemicals during photolithography, making pre-stressed PO a good candidate for a variety of applications.

The Khine Lab has previously utilized the shrink film PO for microfluidic devices,[47,49–53] stem cell growth and formation,[54–58] microlens arrays,[59,60] photolithography,[59,61] and education.[52] When stiff metals are deposited on the surface of PO and the PO is heated, the stiff metals buckle and fold as the PO shrinks, and multiscale (micro to nano) features are formed.[40,42,45] These multiscale wrinkles are currently being used for enhanced point-of-care detection and fluorescent enhancement,[7,42,43,62–65] magnetic trapping,[53] high surface area electrodes,[66] and superhydrophobicity.[6,7] These features can then be imprinted into hard plastics to create superhydrophobic substrates.

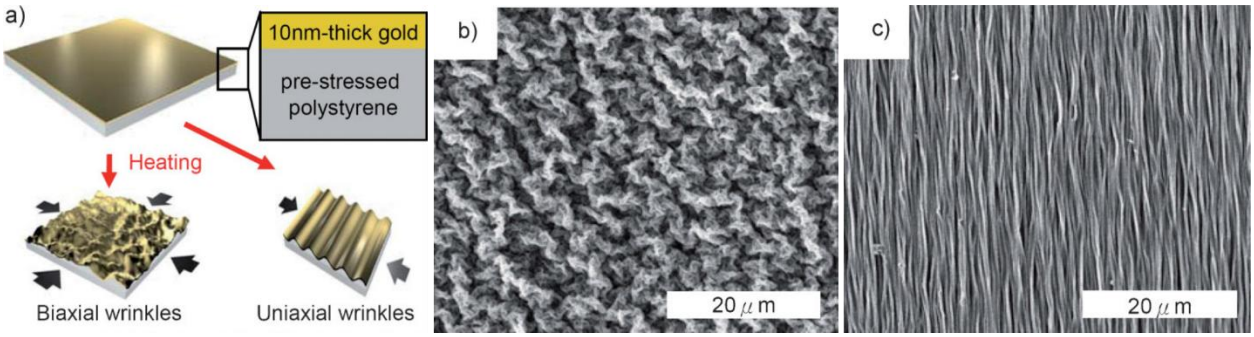


**Figure 2.4**: Uniaxial and biaxial wrinkles are generated by depositing a thin, bimetallic film on the pre-stressed polymer shrink substrate. A) Upon heat, the polymer compresses to yield wrinkles. Micro-to nanoscale features are generated B) biaxially and C) uniaxially.[42]

### *2.3.3 Polymer Manufacturing*

Micro manufacturing techniques such as photolithography have propelled the biomedical engineering field because substrates can be controlled on similar dimensions as the biological systems. Further, utilizing high throughput reproduction techniques at high resolution (such as soft lithography) have enhanced manufacturing techniques, making biological application more practical and accessible.[67–70] PDMS is often used to mold micro and nano features due to its good optical clarity, high resolution molding, gas permeability, biocompatibility, and mechanical properties.[71] Molding with PDMS, however, has its drawbacks as PDMS adsorbs proteins due to its hydrophobic nature.[72] For biological applications, nonspecific protein adsorption is problematic and may interfere was with assays. Other silicones have a decreased amount of protein absorption while maintaining the positive qualities of PDMS,[71] but generally, silicones are not desirable for commercial manufacturing of biomedical products.

Plastics are ideal for manufacturing because they are easily moldable, are inexpensive to produce, can yield high throughput, and have good working temperatures.[73] Common manufacturable plastics are polymethylmetacrylate (PMMA), polycarbonate (PC), polystyrene (PS), and cyclic-olefin copolymer (COC).[73–77]. Plastics can either be manufactured directly or by

replicating features into plastics.[73,75,78] Direct manufacturing techniques include micromachining, injection molding, photopolymerization, and laser ablation.[73,75,78] To replicate high resolution features, thermoplastics can be hot embossed by applying heat and pressure, and plastics can mold with good fidelity.[73–77]

To leverage the advantages of both PDMS and plastics, PDMS can be used as a master to hot emboss micro and nano features into plastics.[75,76] Goral et al. leveraged this novel approach by sandwiching the PDMS master and a sheet of PS between two glass slides, applying pressure with binder clips, and heating the entire device above the glass transition temperature of PS. The PS molds the high resolution features from PDMS, and the PDMS mold can be used for multiple replications. This approach allows for rapid, reproducible plastic devices using a single master mold, and can also be compatible with scale-up manufacturing of hot embossing into plastics.

## 2.4 Superhydrophobic Surface Fabrication

### *2.4.1 Generating Superhydrophobic Wrinkles on Shrink Film*

Superhydrophobic hard plastics were created from the shrink film PO, metal, and hard plastics.[6,7] PO (Sealed Air) was first pretreated with oxygen plasma (SPI Supplies) to temporarily increase the surface energy for better adhesion and was then sputter coated (Quorom) with silver and gold. The PO film was then heated to 160ºC, causing the PO to fully shrink. While the PO shrinks due to heating, the stiff metal film buckles and folds, creating extremely rough, high-aspect, and multiscale structures.[42] When casted with PDMS (Dow Corning Co.), the metallic PO mold transfers its physical shape, producing multiscale roughening on the PDMS surface and enhancing its natural hydrophobic properties (due to Wenzel's and Cassie's equations).

*2.4.2 Imprinting Superhydrophobic Features*

PDMS is further used as a cast because of its thermally and mechanically stable properties. These heterogeneous features are imprinted from PDMS into the inherently hydrophobic hard plastics PS (Grafix Plastics), PC (McMaster-Carr), and PE (McMaster-Carr). To produce structurally modified hard plastics, PS, PC, and PE were casted to the superhydrophobic PDMS mold by applying uniform pressure and heat.[75] Figure 2.5 depicts a process flow of this fabrication method paired with CA images for each step.

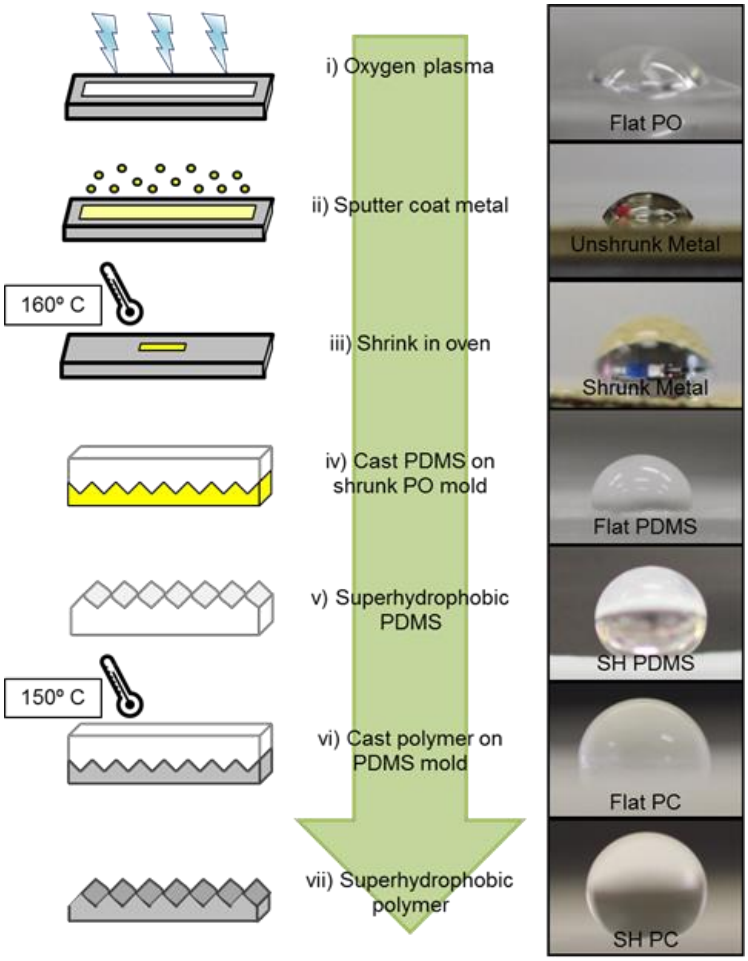


**Figure 2.5**: Process flow of the superhydrophobic substrates formed from shrink film paired with their respective CA images. (i) PO film is plasma treated with oxygen (ii) Treated PO film is sputter coated with silver and gold (iii) PO film is shrunk at 160ºC to induce metal buckling and folding (iv) PDMS is poured over fully shrunk PO film for casting (paired photo features flat PDMS) (v) Superhydrophobic PDMS cast is removed from shrunk PO (vi) Hard plastics are casted into superhydrophobic PDMS mold by applying pressure and heat (paired photo features flat PC) (vii) Superhydrophobic PC casted from superhydrophobic PDMS.

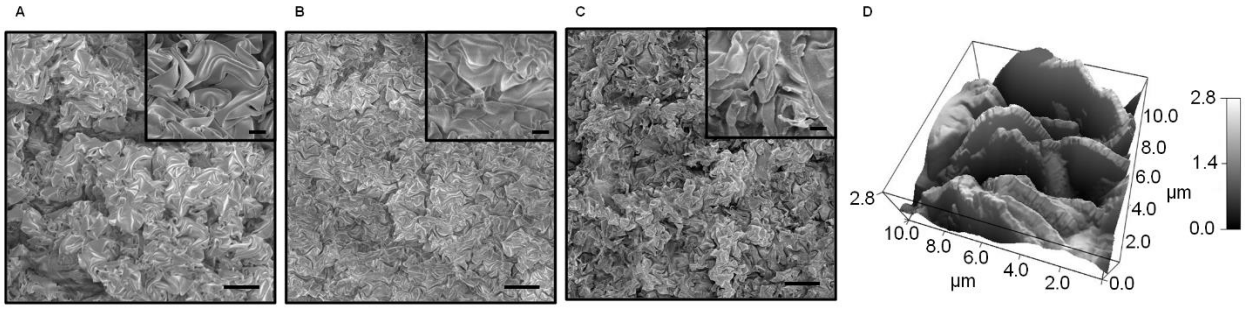


**Figure 2.6**: Top down SEM images and AFM of the structurally modified surfaces' multiscale structures. Features are shown in (A) shrunk, metallic PO, (B) transferred in PDMS, and (C) imprinted in PS from PDMS. Scale bars are 10μm. (D) 3D AFM image of the morphology and height profile.

## 2.5 Superhydrophobic Surface Characterization

### *2.5.1 Micro- to Nanoscale Superhydrophobic Features*

The heterogeneous nano and microstructures of the metal, PDMS, and PS were analyzed using a scanning electron microscope (SEM) (Hitachi S-4700-2 FES) shown in Figure 2.6a-c. The roughness from the shrunk, metallic PO mold is translated directly into the PDMS and subsequently into the PS, PC, and PE. Nanostructures can be seen on the surface of the microstructures, leading to the enhanced hydrophobicity explained by the Cassie-Baxter theory.[8] Further visualization of morphology and height was achieved using Atomic Force Microscopy (AFM) (Asylum MPF3D), shown in Figure 2.6d, displaying a three dimensional view of the shrunk, metallic PO mold with a heterogeneous microstructure height range of 2.8μm and a root mean square (RMS) value of 700nm.

Further, the two dimensional Fast Fourier Transform (2D FFT) was calculated on the SEM images to determine the spatial frequency of the metal, molded PDMS, and embossed plastics PS and COC.[42,79] The SEM images had a scale bar of 1-2μm, and samples had the highest probability at ~1.4μm wavelength. Metal has a second high probability at ~750nm. Data is normalized to the maximum probability in the graph.

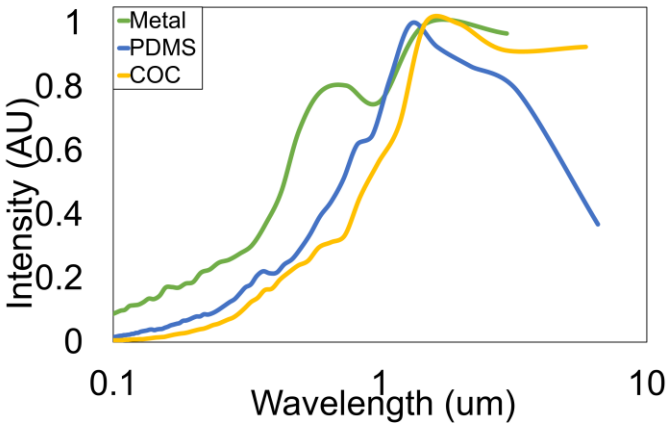


**Figure 2.7**: The FFT graph shows the spatial frequency for the metal, PDMS mold and subsequent mold in COC.

*2.5.2 Contact angle and sliding angle measurements*

The superhydrophobic properties of the structurally modified substrates and the original flat substrates were characterized with CA and SA measurements, as shown in Figure 2.8. A contact angle meter (Drop Shape Analysis System DSA100, KRUSS) was used to measure the CA of initial PDMS molds. Further CA measurements were taken with a drop analysis program[80] on PS, PC, and PE. The SA measurements were performed using a tool clamp with a 90º rotational arm.

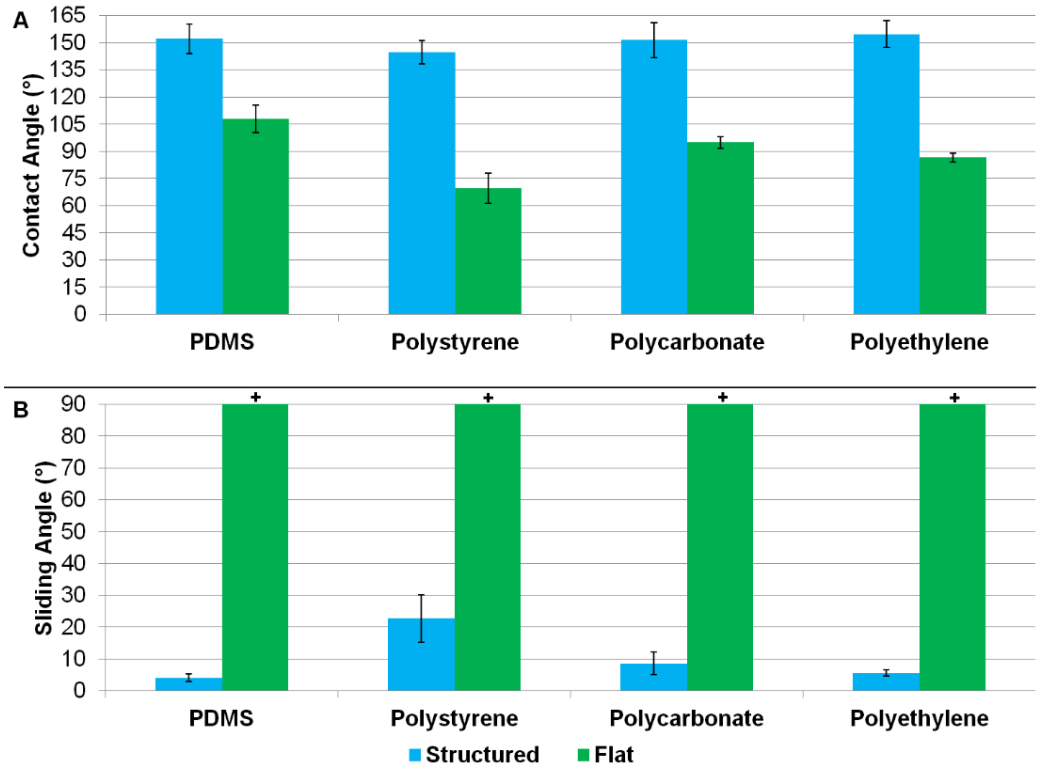


**Figure 2.8**: Graphs depicting CA and SA for the structurally modified surfaces compared to flat. (A) Contact angle measurements of structurally modified and flat PDMS, PS, PC, and PE. (B) Sliding angle measurements of structurally modified and flat PDMS, PS, PC, and PE. + represents measurements >90°.

CA values averaged above 150º with a maximum of 167º measured with the KRUSS system, and the average SA was below 5º with a minimum of less than 2º in PDMS (Figure 2.9). PC and PE yielded similarly high CA values and low SA values indicative of superhydrophobicity. PS produced slightly lower CA values and higher SA values but showed hydrophobic enhancement from its flat comparison. Higher levels of hydrophobicity were achieved through structural modification of initially more hydrophobic polymers (PC and PE) versus initially less hydrophobic polymers (PS). While roughening of the PS surface did increase hydrophobicity, it did not achieve characteristic values to be truly superhydrophobic because of its naturally less hydrophobic state when flat. Thus, for optimal superhydrophobic surfaces, beginning with a more hydrophobic polymer is favorable.

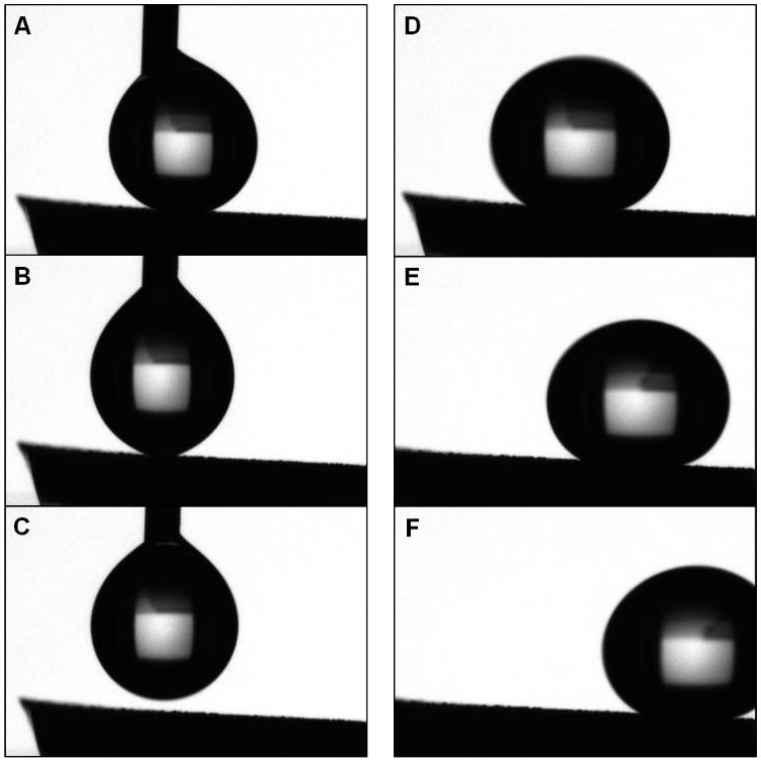


**Figure 2.9**: The low SA of SH PDMS allows the water droplet to easily slide off the surface. (A–C) A droplet being placed on the surface of SH PDMS retracts onto the dropper. (D–F) A droplet sliding off the same surface immediately after placement at a 5˚ angle.

### *2.5.3 Mold Fidelity*

Over the course of three casts from the shrunk, metallic PO to PDMS, the CA remained consistently above 150º (data not shown). In addition, casting PS, PC, or PE from a single PDMS mold has yielded superhydrophobic substrates for more than 100 casts. The effect of temperature on the superhydrophobicity in PDMS molds was also investigated, and superhydrophobicity remained stable across a range of heat exposure from 25-100ºC. PDMS samples were placed on a hotplate at 10°C intervals and allowed to acclimate to the indicated temperature over the course of 5 minutes with a 5 µL water droplet until CA values were taken (data not shown).

*2.5.4 Solid Fraction*

Calculation of the solid fraction $\Phi$ from the Cassie-Baxter equation (3) can be calculated using the average flat CA $\theta_Y$ and the average structurally modified CA $\theta_C$ for each surface (4).

$$\Phi = \frac{\cos\theta_C + 1}{\cos\theta_Y + 1} \tag{4}$$

The solid fraction $\Phi$ is a ratio of the surface contacting the water droplet to the entire structured surface. Since all structures are imprinted from the same initial metal PO mold to the polymers, each polymer would theoretically have the same solid fraction $\Phi$. However, the initial $\theta_Y$ is different for each polymer due to intrinsic chemical differences, causing slight variation in $\Phi$ between materials. Table 2.1 shows calculated values of $\Phi$ for our roughened substrates. The low values are similar to the findings of Zhu et al. whose calculated $\Phi$ was typically less than 0.1, indicating a highly structured surface.[81] As apparent from equations 3 and 4, as $\Phi$ approaches 0, $\theta_C$ approaches 180°.

**Table 2.1**. The solid fraction $\Phi$ was calculated using the average flat CA $\theta_Y$ and the average structurally modified CA $\theta_C$ for each material. A low value of $\Phi$ represents minimal water contact with the surface.

| Material | $\theta_C$ (°) | $\theta_Y$ (°) | $\Phi$ |
|---|---|---|---|
| PDMS | 152 | 108 | .17 |
| PS | 145 | 70 | .14 |
| PC | 151 | 95 | .14 |
| PE | 155 | 87 | .09 |

## 2.6 Summary

Here, we have presented a novel method of producing a superhydrophobic surface from PO by simply molding our unique multi-scale features into PDMS and again into hard plastics such as PS, PC, and PE. This process is rapid, reproducible, and eliminates the need for post processing of chemical alterations to the surface. These superhydrophobic surfaces become much more robust due to the reliance solely on physical geometry at the surface. In addition, using PDMS as a means to transfer the SH micro- to nanoscale structures presents the opportunity to produce a substantial number of superhydrophobic hard plastics from a single mold. Finally, this technique is compatible with roll-to-roll manufacturing and scale-up production methods due to the use of polymers, making this process potentially accessible for many different applications.

# CHAPTER 3: Scale-up Manufacturing of Superhydrophobic Surfaces

## 3.1 Current Fabrication Approaches

Due to their unique properties, SH surfaces have been used for bacterial prevention, drag reduction, non-adhesion, energy conservation, and green energy.[6,20,21,82,83] A SH surface has a low surface energy as well as micro- to nanoscale features, which are often achieved through a combination of chemical and structural modification. To lower the surface energy, fluorocarbon and hydrocarbon chemicals can be deposited on roughened surfaces to achieve superhydrophobicity.[35,36,84] Additionally, surfaces with low surface energies can be structurally roughened using a variety of techniques such as plasma etching, chemical etching, lithography, sol-gel processing, laser ablation, electrospinning, crystallization, and oxidation.[23,36,85–89]

However, these production methods are often complex, expensive, serial, and require post-processing, preventing mass scale manufacturing.[20,21,82] Therefore, commercial applications of SH surfaces heretofore have been limited.[90,91] Furthermore, the addition of hydrophobic chemicals are often not desirable for food or medical applications. A common mass manufacturing technique that yields high throughput is roll-to-roll (R2R) processing where alterations to a surface are performed in a single, quick process on a large roll of a material.[92,93] Originating from the printing industry, R2R manufacturing is nowadays widely used in printed electronics and printed diagnostics applications for high-volume, low-cost manufacturing of disposable components and can be performed in a variety of materials such as thin films, flexible polymers, and conformal tapes.[94] The ability to inexpensively manufacture large areas of SH surfaces without chemical modifications with high throughput and high fidelity would enable SH surfaces for a wide range of medical and healthcare applications.

## 3.2 Roll-to-Roll Manufacturing

### *3.2.1 Flatbed Superhydrophobic Surfaces*

As described previously, SH surfaces have been developed by depositing a thin layer of silver and gold on the pre-stressed polymer PO.[6,7] Upon shrinking the pre-stressed polymer substrate, the mismatch in elastic moduli between the stiff metals and polymer yields a hierarchy of features supportive of superhydrophobicity.[6,7]

Next, the fabrication protocol becomes compatible with scale-up manufacturing by depositing a thin layer of stiff material on the pre-stressed polymer in a R2R platform. Since gold was not a viable material to deposit R2R and because a bimetallic layer is necessary to form SH wrinkles, a combination of materials compatible with R2R deposition was first characterized in a sheet evaporation setup. Combinations of zinc, copper, and calcium were paired with silver due to the high Young's modulus of each material. The deposition of silver (Ag) and calcium (Ca) on pre-stressed polystyrene (PS) was chosen as the optimal deposition materials, and the process flow of fabricating SH wrinkles in hard plastics is shown in Figure 3.1.

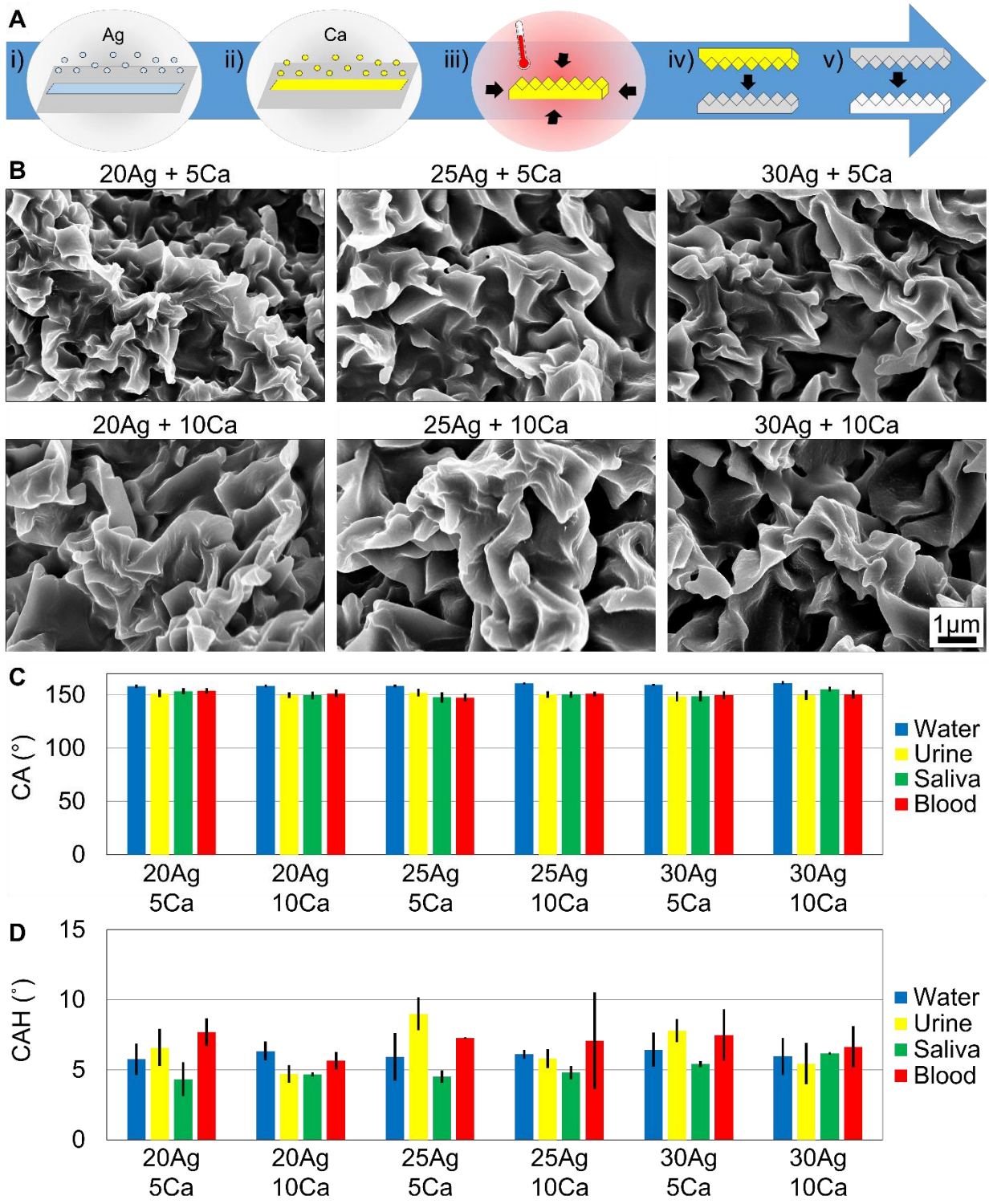


**Figure 3.1**: Sheet evaporation on PS was characterized with 20nm Ag + 5nm Ca, 20nm Ag + 10nm Ca, 25nm Ag + 5nm Ca, 25nm Ag + 10nm Ca, 30nm Ag + 5nm Ca, and 30nm Ag + 10nm Ca. A) i) Silver is first deposited, ii) then calcium is deposited in sheet evaporation. iii) The SH features are formed while shrinking the metalized film, and the SH features are iv) molded into an intermediary silicone and v) embossed into plastic to achieve the final product. B) SEM images of the hierarchical features in plastic show hierarchical winkles. Scale bars are 1µm for all images. C) CA of water and bodily fluids on all conditions are SH. D) CAH of water and bodily fluids on all conditions are SH.

To further optimize SH wrinkles, the deposition ratio of silver to calcium was characterized.[6,7] Figure 3.1b shows Scanning Electron Microscopy (SEM) images of the features from shrunk PS with 20nm Ag + 5nm Ca, 20nm Ag + 10nm Ca, 25nm Ag + 5nm Ca, 25nm Ag + 10nm Ca, 30nm Ag + 5nm Ca, and 30nm Ag + 10nm Ca deposited. All features yielded micro- to nanoscale structures, imprinted into hard plastics with high fidelity, and demonstrated superhydrophobicity. Figure 3.2a graphs the Fast Fourier Transforms (FFTs) and shows the spatial frequency of the SH features on the sheet evaporation. The SEM images had a scale bar of 2μm, and all samples had the highest probability at ~750nm wavelength, indicating that these features are tighter than initial features. Data is normalized to the maximum probability in the graph.

Figure 3.1c-d graph the CA and CAH of water, urine, saliva, and blood on the six deposition conditions molded into the hard plastic polypropylene (PP). Water has a CA greater than 150˚ for all substrates, and the CA of water ranges from 158˚ ± 4˚ to 161˚ ± 5˚. Urine, saliva, and blood also have SH CA values on the six different deposition conditions. CA values of urine range from 149˚ ± 8˚ to 152˚ ± 7˚. CA values of saliva range from 148˚ ± 8˚ to 156˚ ± 4˚. CA of blood range from 148˚ ± 6˚ to 154˚ ± 4˚. Note that standard deviations overlap, and conditions are not statistically different.

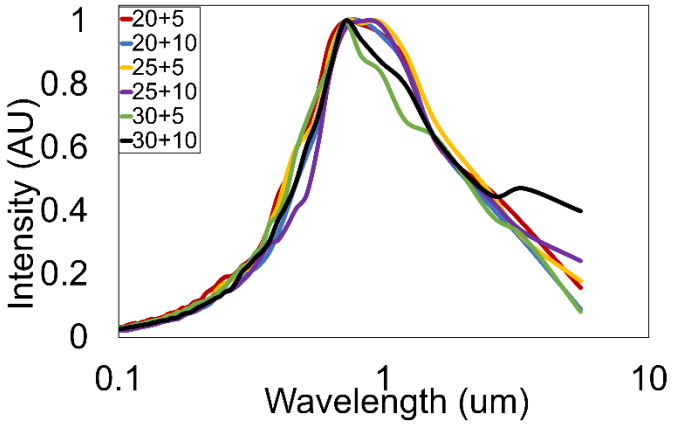


**Figure 3.2**: The FFT graph shows the spatial frequency for the sheet evaporation, and wavelengths have the highest probability ~750nm.

CAH values were measured by taking the difference in advancing and receding CA values. CAH values are also indicative of superhydrophobicity for water, urine, saliva, and blood. CAH values for water range from 6˚ ± 2˚ to 9˚ ± 4˚. CAH values for urine range from 5˚ ± 1˚ to 9˚ ± 2˚. CAH values for saliva range from 4˚ ± 1 to 6˚ ± 1˚. CAH values for blood range from 6˚ ± 1˚ to 8˚ ± 2˚.

The 20nm Ag + 5nm Ca deposition was chosen as the optimal condition because superhydrophobicity is consistently achieved for all fluids (i.e. CA >150˚ and CAH <10˚). The 20nm Ag + 5nm Ca deposition also requires the least amount of materials and is the most beneficial for manufacturing.

### *3.2.2 Roll-to-Roll Superhydrophobic Surfaces*

Next, R2R deposition on pre-stressed PS was performed, and SH features were created in a R2R platform. Figure 3.3a shows the process flow of R2R production. Silver and calcium are deposited on a pre-stressed roll of PS. Sections of the roll are shrunk, and the SH features are imprinted into silicones and hard plastics as the final product. Figure 3.3b-c show the R2R deposition equipment and the actual size of the metalized roll, shrunk master, and molded PP product. The fidelity of the roll was tested by characterizing the front, middle, and rear of the roll.

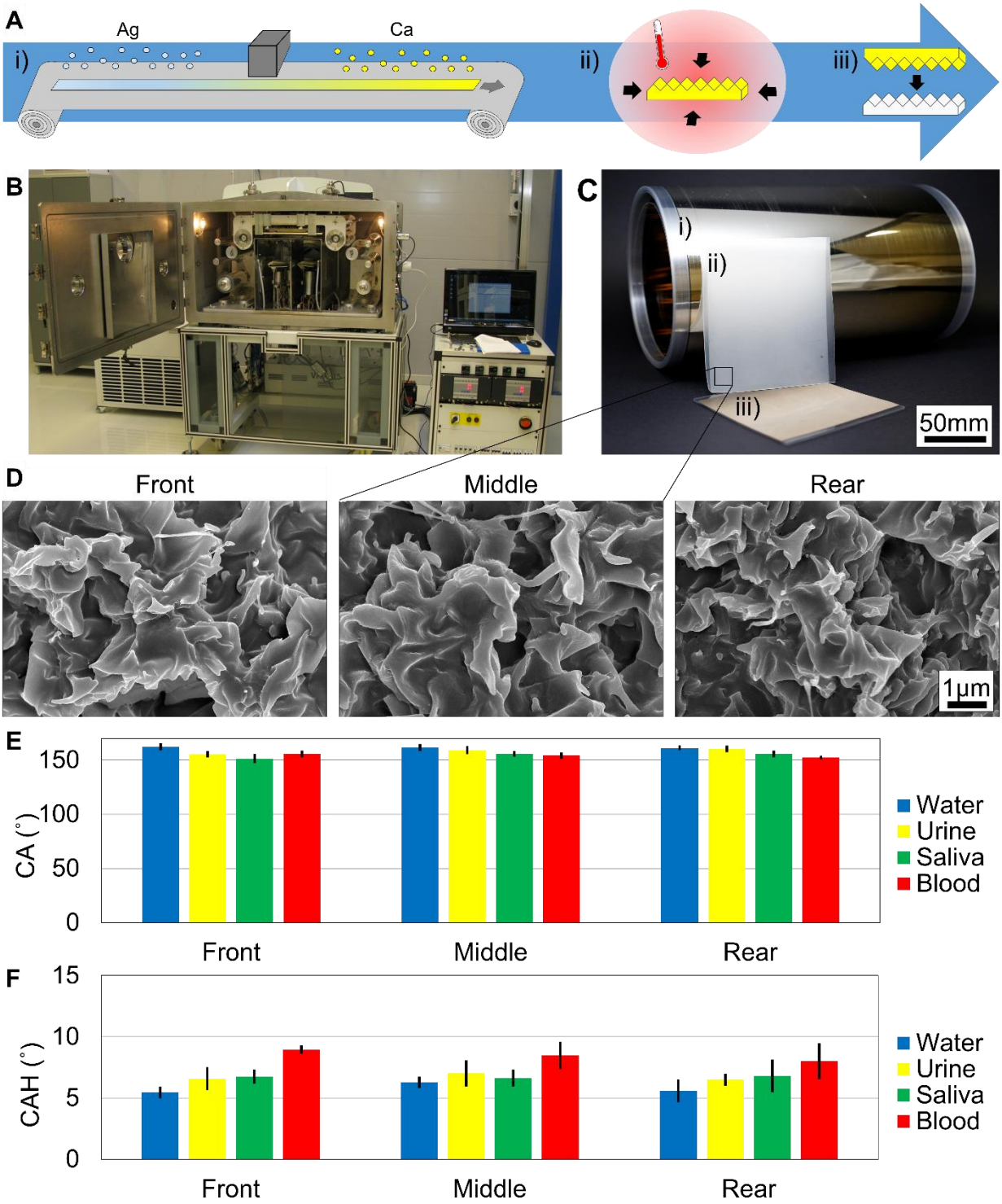


**Figure 3.3**: SH surfaces are fabricated in a R2R platform. A) i) 20nm Ag, then 5nm Ca are deposited on the pre-stressed PS film in a R2R deposition chamber, ii) the metalized PS shrink film is shrunk to achieve SH features, and iii) the SH features are imprinted into hard plastics. B) Materials are deposited on the shrink film in the VTT EVA R2R Evaporator Line. C) (i) A roll of metalized shrink film is 30cm x 300m. (ii) The metal film is shrunk), and (iii) large SH hard plastics are created. D) SEM images of the front, middle, and rear of the metalized PS roll were tested to show the consistency of deposition throughout the roll. Scale bars are 1µm for all SEM images. E) CA of water, urine, saliva, and blood on all conditions are SH. F) CAH of all fluids are SH on all conditions.

Figure 3.3d shows the SEMs of the mico- to nanoscale features of the front, middle, and rear of the roll. Features are consistent throughout the roll, and therefore metal deposition and superhydrophobicity are consistent throughout the roll. Figure 3.4a graphs the FFTs of the spatial frequency of the SH features on the R2R deposition, and the spatial frequency yields the highest probability at ~750nm. Figure 3.4b overlays the 20nm Ag + 5nm Ca FFT from the sheet evaporation with the FFT data for the front, middle, and rear of the R2R roll to show that wrinkle features are similar with heterogeneous variation. The SEM images had a scale bar of 2µm, and all samples had the highest probability at ~750nm wavelength. R2R features are comparable to the sheet evaporation features, and the R2R has tighter features compared to the initial small-scale fabrication method. Data is normalized to the maximum probability in the graphs.

Figure 3.3e-f graph the CA and CAH values for water, urine, saliva, and blood tested on the front, middle, and rear of the roll. CA and CAH values for water and bodily fluids are indicative of superhydrophobicity. The average CA values are 162˚ ± 5˚ for water, 158˚ ± 6˚ for urine, 154˚ ± 6˚ for saliva, and 154˚ ± 5˚ for blood.

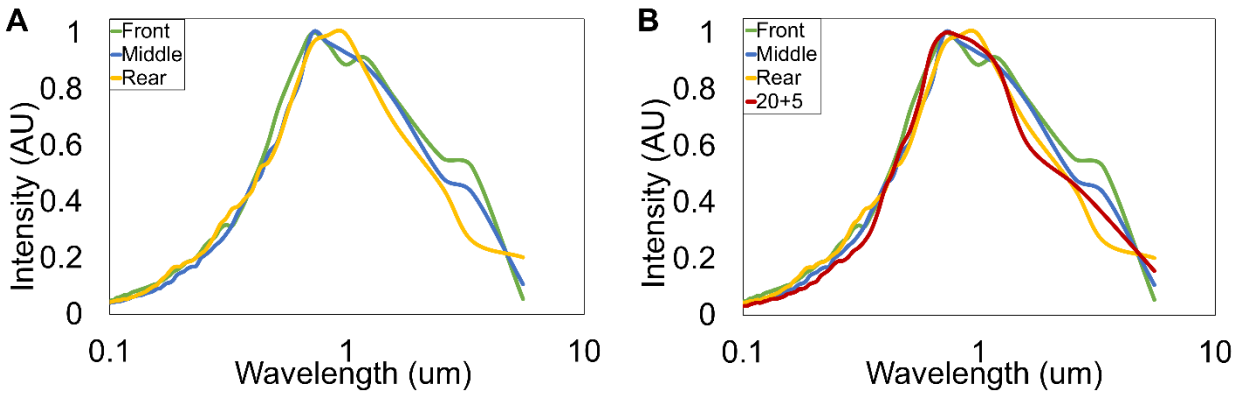


**Figure 3.4**: The FFT graphs show the spatial frequency for the A) R2R and B) R2R overlayed with the 20+5 condition from the sheet evaporation.

CAH values average 6˚ ± 1˚ for water, 7˚ ± 1˚ for urine, 7˚ ± 1˚ for saliva, and 9˚ ± 2˚ for blood. The standard deviation of the front, middle, and rear of the roll overlap for CA and CAH values for each fluid, confirming that superhydrophobicity is consistent throughout the roll. Note that CAH values for saliva on the R2R surfaces are greater than CAH values on the sheet evaporation surfaces. The surface tension of saliva, however, is shown to fluctuate between 45mNm$^{-1}$ to 69mNm$^{-1}$ depending on when subjects drank water prior to collection and also the time of testing post collection.[95] The CA and CAH can be dramatically affected by such fluctuation but notably, values are consistently indicative of superhydrophobicity on the R2R surfaces.

### 3.3 Summary

SH surfaces are created in a R2R platform with high fidelity and high throughput. The purely structural modification allows for inexpensive embossing into any commercially-available and FDA-approved plastic for medical applications, and post processing is not necessary. The SH surfaces are phobic to water, blood, urine, and saliva. The proposed SH biomaterial is biocompatible and can therefore function as an effective material for a plethora of medical applications, for example, as catheters and medical tubing.

# CHAPTER 4: Superhydrophobic Surfaces for Antibacterial Applications

## 4.1 Introduction

### *4.1.1. Bacterial Infections*

The spread of bacteria is a common problem and is the main source of health associated infections. In 2009, such health associated infections cost the healthcare industry $28-45 billion and ranged from food poisoning to septicemia, often leading to extensive hospital care and even death.[96–98] Bacterial exposure can occur during surgical procedures or can be transferred patient-to-patient from infected hospital surfaces.[98] Hospitals are a major source of bacterial spread, but everyday facilities also act as distributors of bacterial disease. Flores et al. has shown that public restrooms house at least nineteen strains of bacteria, ranging from skin, gut, and soil sources that can be transferred by touch.[99] Furthermore, multiple bacterial strands are capable of growing on plastics and fabric surfaces for days and even months.[99–101] Therefore, there is a growing demand for reliable antibacterial surfaces to combat this common occurrence of contamination.

### *4.1.2 Antibacterial Agents*

Currently, there are fabrication methods for antibacterial reagents and structurally modified antibacterial surfaces. Silver nanoparticles have been used as a bacterial growth inhibitor as the heavy metals disrupt and inactivate the proteins in bacteria, preventing growth.[102,103] Functional groups on self-assembled gold monolayers have also been used to decrease bacterial motility and attachment, preventing cell adherence, growth of bacteria on surfaces, and the formation of biofilms.[104] Zheng et al. has shown that high molecular weights of chitosan inhibit gram-positive bacteria such as *Staphylococus aureus* due to lack of nutrient adsorption whereas low molecular weights of chitosan inhibit gram-negative bacteria such as *Escherichia coli (E. coli)* due to a

disturbed metabolism.[105] Chemically modified superhydrophobic surfaces have also been shown to inhibit bacterial growth because of the low surface energy and minimal contact with the surface for bacterial adhesion.[33] While many antibacterial reagents and chemicals effectively inhibit the growth of bacteria, they can lead to bacterial resistance and become ineffective over time.[106] Purely structural antibacterial surfaces, however, do not induce bacterial resistance and are therefore ideal for preventing the spread of infectious bacteria. Superhydrophobic surfaces have become particularly desirable as stable antibacterial surfaces because of their self-cleaning and water resistant properties.

Thus, leveraging these superhydrophobic surfaces for antibacterial applications is feasible. Due to the minimal solid-liquid contact, the inherently low surface energy of the material, and low SA of the substrate, bacteria prefer to remain in solution rather than adhere to the surface.[107,108] When a droplet containing bacteria contacts a superhydrophobic surface, there is minimal contact where the bacteria can adhere to the surface. Additionally, in this low contact area, there is low surface energy which allows only weak interactions between the surface and bacteria, preventing strong bacterial adhesion.[109] Since the superhydrophobic surface also has a low SA, bacteria in solution easily slide off the surface when tilted and do not adhere to the surface. Privett et al. even show that structural modification dominates over chemically modified hydrophobic surfaces such as fluorination for antibacterial properties.[33] With solely a structural modification, a superhydrophobic surface will repel bacteria in solution rather than kill them, negating the potential for resistance as would occur due to chemical reagents.

### 4.2 Reduced Bacterial Adhesion on Superhydrophobic Surfaces

Antibacterial testing was performed on PS, PC, and PE samples for both flat and SH substrates using DH5-α gram-negative *E. coli*. Plating concentrations were determined as 100,100 colony forming units per mL (CFU)/mL for PS and PC and 25,800 CFU/mL for PE. For testing antibacterial properties, 10µL of bacterial solution was placed on the surface of each substrate. Substrates were tilted at 90° to allow bacterial solution to roll off, if possible. Subsequently, samples were either rinsed with sterile phosphate buffered saline (PBS) or not rinsed. The surfaces of the substrates were then stamped face-down in agar plates (Fisher Scientific) to transfer residual bacteria. 10µL of bacterial solution was added directly to the control agar plates.

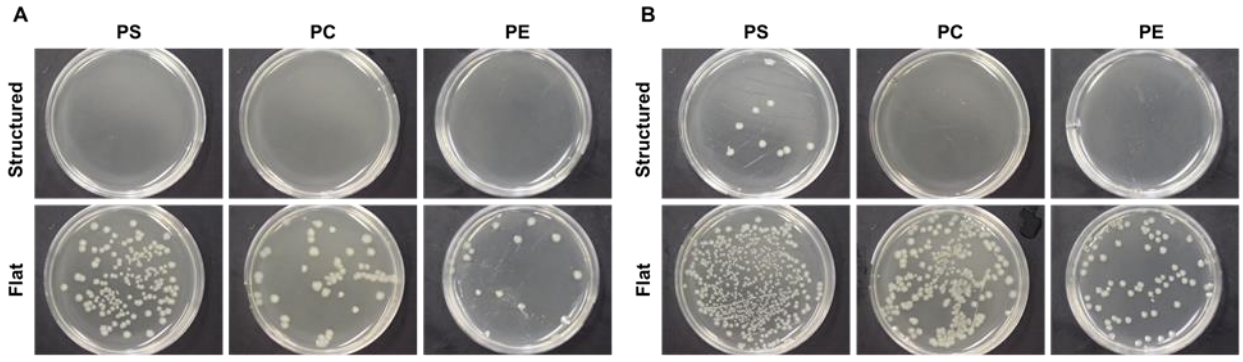


**Figure 4.1**: PS, PC, and PE structured and flat substrates were contaminated with a bacteria solution, either rinsed or not rinsed, and transferred to agar plates. The resulting bacterial growth can be observed in each plate as colonies. (A) Substrates were rinsed with PBS after bacteria solution was deposited on the surface. (B) Substrates were not rinsed.

Superhydrophobic surfaces exhibit a significantly reduced amount of bacterial growth compared to flat surfaces, as shown in Figure 4.1. Rinsed superhydrophobic surfaces yielded <100 CFUs for PS and PE, and no bacteria was observed on rinsed superhydrophobic PC (Table 4.1). The flat rinsed surfaces had much higher CFU counts where 10% of the initial number of cells was transferred to the agar plates. The no rinse superhydrophobic surfaces were also effective at preventing bacterial adhesion with only ~2% of the original number of cells plated in the final CFU count. Not rinsed flat surfaces had >34% of the original number of bacteria plated. Note that all samples experienced a loss of bacteria due to gravity during the tilting step of the experiment.

Overall, bacterial adhesion on the SH surfaces was decreased >20x compared to flat without rinsing, purely due to the low adhesion properties of the SH surfaces. With rinsing, bacterial adhesion was reduced >150x compared to flat due to the self-cleaning behavior of SH surfaces. Total bacterial adhesion was reduced >1500x on the SH surfaces compared to >10x on the flat surfaces.

**Table 4.1**: CFU counts for structured versus flat surfaces.
*One agar plate yielded a condensed area of cell growth, hindering the ability to count individual colonies. Thus, this value is an underestimate.

| Condition | Substrate | PS | PC | PE | % Adherence (Average of Condition/Control) |
|---|---|---|---|---|---|
| Rinse | Structured | 70 | 0 | 30 | <0.1% |
| | Flat | 15,700 | 10,700 | 900 | 10% |
| No Rinse | Structured | 2,100 | 1,500 | 300 | 2% |
| | Flat | >36,900* | 30,700 | 8,900 | >34%* |
| Control | Control | 100,100 | 100,100 | 25,800 | 100% |

### 4.3 Summary

SH surfaces are antibacterial because of their minimal solid-liquid contact at the surface, weak surface interactions with bacteria, and low SA. As a result of these properties, it is energetically favorable for the bacteria to remain in solution and to roll off the surface when tilted rather than adhere to the SH surface. This self-cleaning principle is the key to antibacterial properties of SH surfaces. Dirt and bacteria adhere to water better than the surface and are, therefore, cleaned easily by simple rinsing, mitigating the need for antibacterial reagents. Since this antibacterial design is purely structural, a product with permanent features can be manufactured for everyday use with minimal maintenance for the customer.

# CHAPTER 5:

# Superhydrophobic Surfaces for Enhanced Point-of-Care Diagnostics

## 5.1 Point-of-Care Diagnostics

Point-of-care (POC) diagnostics aim to shorten the gap between patients and medical tests by making sensitive diagnostics more affordable and accessible. With more accessible devices, diseases can be detected at their onset, and patients can attain faster and more successful treatment. Bodily fluids such as urine are ideal mediums for POC devices because sample collection is non-invasive, poses minimal threat to the patient, and can be performed frequently for temporal resolution. However, the low concentration of biomarkers in urine begs the need for highly sensitive devices for accurate detection. To detect low concentrations, biosensors often employ complex features such as nanoparticles[110–112] and structured surfaces[63,113,114] with equipment intensive amplification methods such as surface plasmon resonance[43,62,115] to enhance the detection signal. Another approach for enhanced detection is increasing the concentration of biomolecules to a range detectable using standard techniques (such as a colorimetric output). One simple, low-cost approach to increase the concentration is to evaporate molecules on a superhydrophobic (SH) surface.

## 5.2 Evaporation on Surfaces

### *5.2.1 Evaporation on a Flat Surface*

As a droplet of water sits on a surface, fluid will evaporate into the atmosphere at the air-liquid interface.[116–120] As the volume decreases due to evaporation, the balance of interfacial forces is constantly changing, causing capillary flow within the droplet and driving particles to the droplet's contact line.[116–118] On a flat surface, the water droplet's strong adhesion to the surface pins the

volume of fluid to the initial footprint, and the contact line remains constant. When fluid is completely evaporated, the particles have flowed to the edge of the droplet and are contained at the droplet's contact line, known as the coffee ring effect.[116,117]

### *5.2.2 Laplace Pressure*

The size of the water droplet on a surface affects the adhesion properties between the solid and liquid because of the droplet's internal Laplace pressure, which can be quantified by

$$\Delta P = \frac{2\gamma}{R} \tag{1}$$

where $\gamma$ is the surface tension of the fluid, and $R$ is the radius of the droplet.[22,121]

As the size of the droplet decreases, the internal pressure increases, which can alter the droplet from being in the Cassie-Baxter regime (air pockets between the solid and liquid with minimal adhesion to the surface) to the Wenzel regime (no air pockets with maximum adhesion to the surface). As the internal pressure increases, the balance of forces is continually changing, and the water droplet can change from balancing on the peaks of the surface (Cassie) to sinking into the multiscale structures (Wenzel).[22,122–124] A water droplet can naturally transition from Cassie to Wenzel due to a change in internal droplet pressure.

### *5.2.3 Evaporation on a Superhydrophobic Surface*

When a droplet of fluid evaporates into the atmosphere on surface, the balance of forces at the air-liquid interface constantly increases the droplet's surface tension and applies an inward force at the droplet's contact line (air-liquid-solid interface).[118] On a SH surface, the droplet's inward pulling force (due to the localized increase in surface tension) is greater than the droplet's adhesion to the surface, and the droplet's contact line continually moves inward, creating a smaller footprint

and contact diameter for the droplet,[118–120,125–128] as shown in Figure 5.1. Therefore, as volume decreases, contact area also decreases due to pinning and depinning of water.[125,126]

The pinning and depinning can be attributed to the change in surface tension during evaporation and the peaks in the Cassie-Baxter phenomenon. As the water evaporates and the volume decreases, surface tension locally increases at the three phase interphase, and the contact angle slightly decreases at the edge of the surface-liquid interface. When this increased surface tension has enough force to pull the water droplet inward, the water depins from the edge of the peaks of the SH surface. As the water droplet is pulled inward, the surface tension relaxes, and the CA slightly increases. The droplet then repins to a new peak of the SH surface and momentarily maintains equilibrium. As the droplet continues to evaporate, the droplet depins and repins, thus decreasing the contact area of the water droplet with the surface.

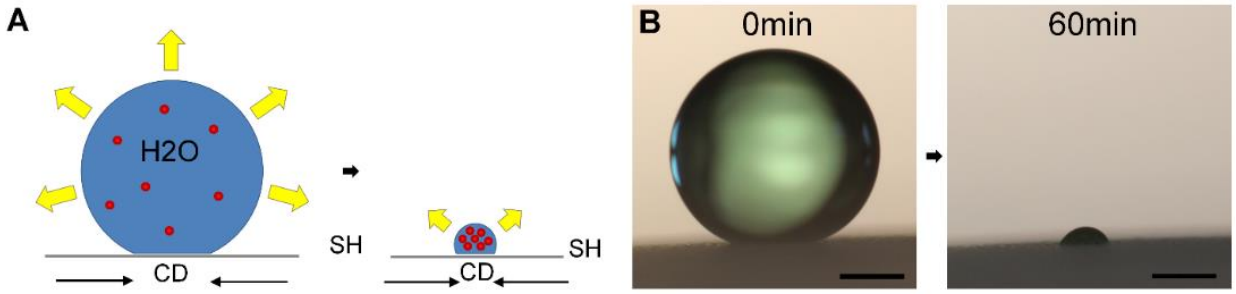


**Figure 5.1**: Evaporation on a SH surface. (A) Fluid evaporates from the SH droplet at the air-liquid interface, and particles concentrate. (B) The dimensions of a SH droplet containing food dye shrink during evaporation, concentrating molecules to a small footprint area. Scale bars are 500μm.

Eventually, this pinning and depinning ends when the water droplet collapses into its final footprint. As the volume decreases, the Laplace pressure increases, and the pressure of the water droplet overcomes the upward force from the air pockets.[22,122] Fluid then collapses into the micro- and nanoscale features of the surface and permanently pins to the surface (i.e. transitions from the Cassie-Baxter to the Wenzel state). Fluid will stay pinned at this reduced contact area until evaporation is complete. This reduced contact area contains the content of the droplet with the molecules concentrated only on a small footprint. **Figure 5.2** overlays time lapse images of a droplet of green food evaporating. As fluid evaporates, the green molecules concentrate, and the contact footprint decreases. Finally, the molecules collapse into a small footprint.

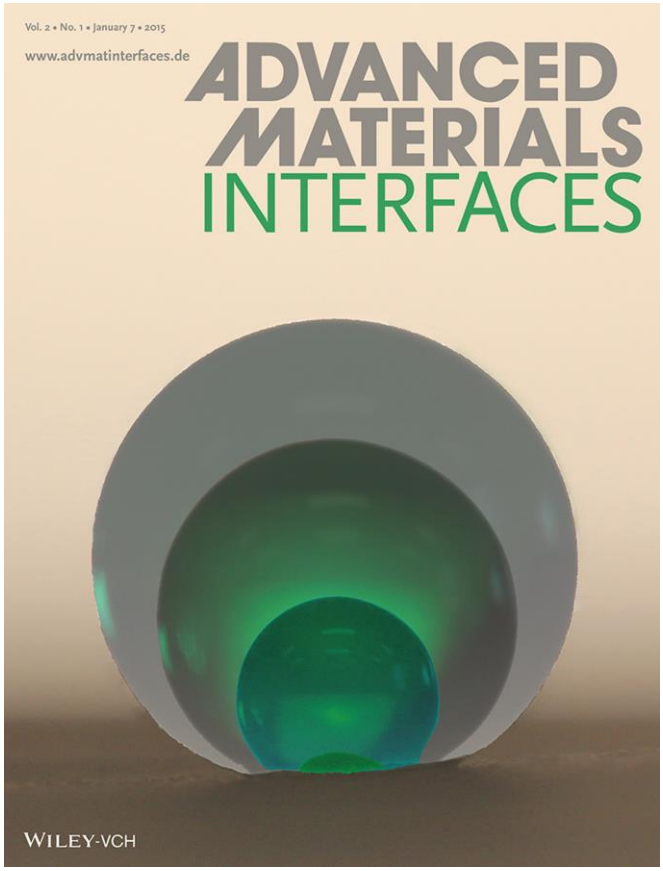


**Figure 5.2**: Time lapse images of a droplet of green food dye evaporating. The footprint decreases as molecules concentrate to a final pellet.[7]

This simple approach enables large concentration increases compared to a flat surface.[119,120,125,129] McLauchlin et al. show a 5-fold improved sensitivity of protein detection by evaporating droplets on a patterned hydrophilic-superhydrophobic substrate.[120] Choi et al. has characterized droplet evaporation on their SH surfaces and has shown compatibility with biological fluids, claiming their device has potential to enhance biological detection.[119] Using evaporation on a SH surface and surface enhanced Raman spectroscopy (SERS) techniques, 4.8agmL$^{-1}$ ($10^{-18}$) of Rhodamine and a single strand of lambda DNA have been detected.[125,129] While these approaches are promising, they are either still lacking in detection sensitivity or too costly and complex for POC diagnostics. Thus, there is still a need for enhanced sensitivity while minimizing detection costs to enable true zero-cost diagnostics.

## 5.3 Characterization of Evaporation on a Superhydrophobic Surface

### *5.3.1 Droplet Characterization*

First, water droplet parameters are characterized at time point zero (i.e. no evaporation). Larger volumes have larger diameter (D), height (H), and contact diameter (CD) (Figure 5.3a). With the increasing volume, the droplet's mass increases, and the effect of gravity is more noticeable. As expected, the droplet's height increases less dramatically than the diameter, and larger droplets have a lower H/D ratio compared to small, more spherical droplets with H/D approaching 1. Calculated volume is consistent with the applied volume (Figure 5.3b). Large volumes of water have relatively low and constant Laplace pressures ranging from 46-69Pa for 50-200µL. As the volume decreases, the internal droplet pressure dramatically increases, and a 2µL droplet has a pressure greater than 200Pa. CA remains above 150° for all volumes, indicating that the balance of forces at the contact line maintains superhydrophobicity for all volumes shown (Figure 5.3c).

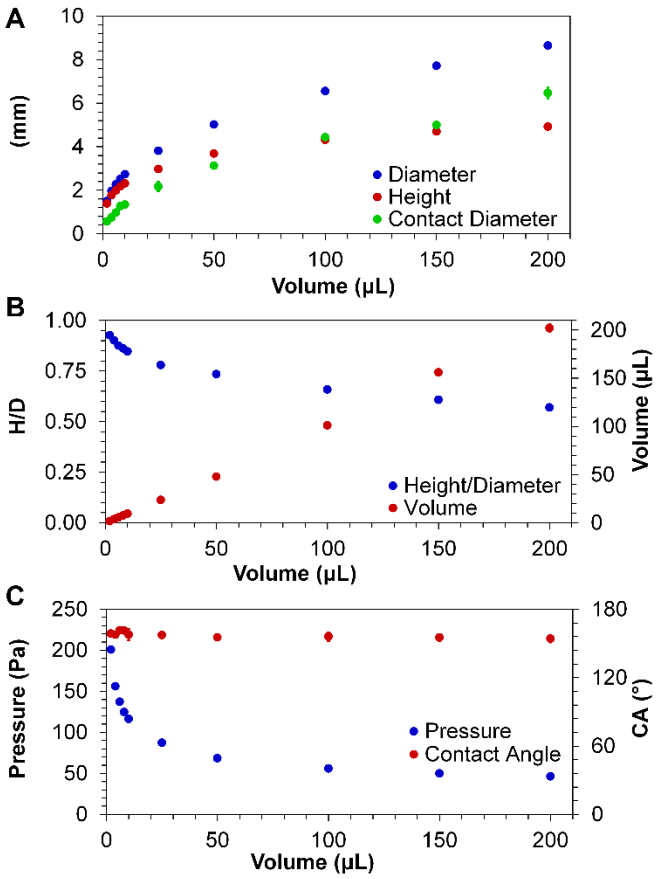


**Figure 5.3**: Droplet characterization. (A) As the droplet's volume increases, the droplet's diameter, height, and contact diameter increase. (B) The H/D ratio decreases as volume increases due to the mass. Calculated volume compares with deposited volume. (C) Internal droplet pressure increases as the volume decreases, and the CA consistently stays above 150° for all volumes. N = 3

### *5.3.2 Evaporation of Water*

Figure 5.4 shows images of water droplets of various volumes evaporating over time, and Figure 5.5 shows the characterization of water droplet evaporation over time for 1-20µL. Water completely evaporates, and nothing is left on the SH surface. Larger volumes take longer to evaporate (30min for 1µL compared to 180min for 20µL). The droplet dimensions such as diameter, height, CD, and calculated volume also decrease as a function of time. Indicative of a SH surface, the CD decreases during evaporation because the surface is in the SH Cassie regime. The volume at which the CA falls below SH values (i.e. transitions from Cassie to Wenzel) is

~300nL, and the corresponding transition pressure is ~360Pa. This internal pressure overcomes the upward force of air trapped beneath the water droplet and allows the fluid to collapse into the multiscale features (i.e. pin to the surface). This pressure is similar to the pressures used by Lafuma and Quere (~250Pa),[22] showing that our substrates can withstand high pressures before transitioning. Eventually, all water evaporates into the atmosphere, and no footprint remains for pure water. Multiple experiments were performed on the same substrate, and all data yielded SH characteristics, showing that the transition from the Cassie to the Wenzel regime is reversible once fluid is completely evaporated and air pockets are present.

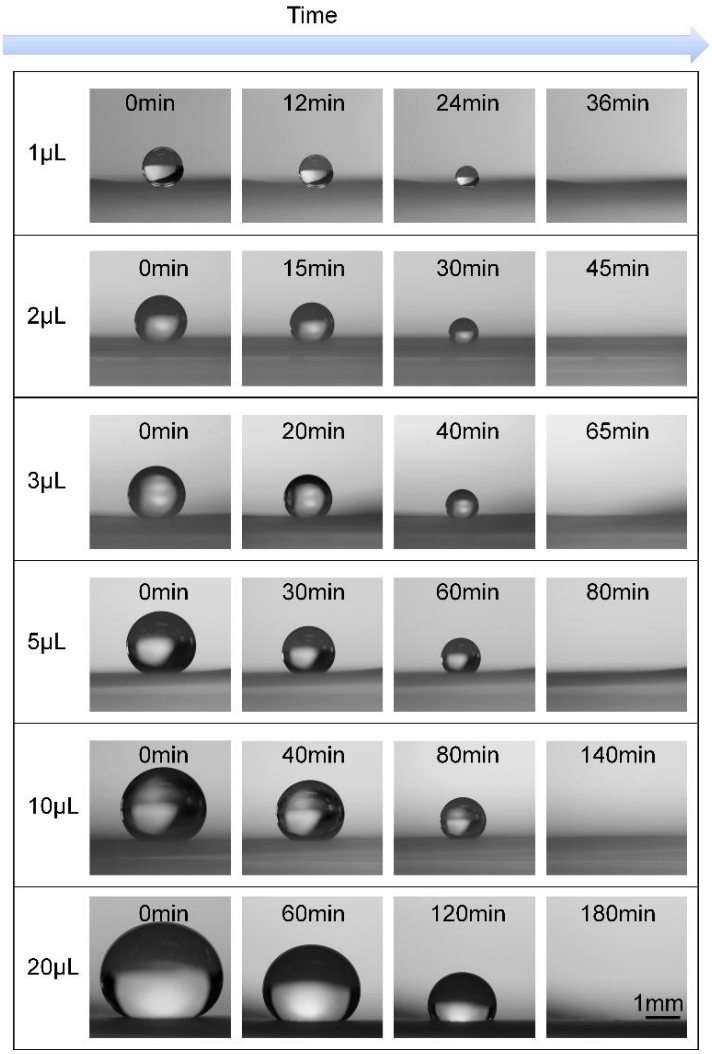


**Figure 5.4**: Images of pure water droplet evaporation. The droplet's diameter, height, contact diameter, and volume decrease, but the CA remains SH. Eventually, the droplet completely evaporates.

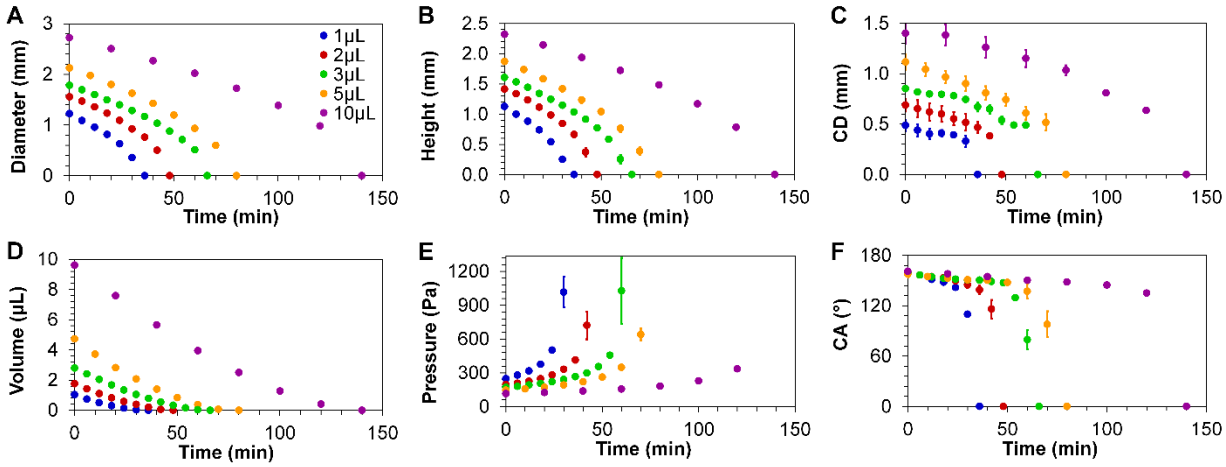


**Figure 5.5**: Characterization of water evaporating on a SH surface. A) Diameter, (B) Height, (C) Contact Diameter, (D) Volume, I Pressure, and (F) Contact Angle of water during evaporation. N=3

### *5.3.3 Evaporation of BSA*

Bovine serum albumin (BSA) is used as a model protein, and evaporation of 2µL of BSA is compared to evaporation of 2µL of water (larger volumes are not graphically compared). After all solution evaporates from the droplet, the BSA particles reside as a pellet on the SH surface in a confined footprint (defined by the final CD). All concentrations of BSA solutions have similar evaporation rates and dimensions as pure water (Figure 5.6). The diameter is similar to water for all concentrations of BSA, and the height of all BSA droplets is consistently lower than water. Low concentrations of BSA have similar CD, but higher concentrations have higher CD due to the presence of molecules increasing interacts with the surface. CA values remained SH for BSA until pressures were large enough to pin the droplet to the surface (~250Pa). The droplet volume decreases from 1.97±0.02µL to 4.9±1.7nL (at the time frame before evaporation is complete), and particles concentrate at least 171x with a maximum of 405x. In addition, the average contact area decreases from 0.41±0.06mm$^2$ to 0.09±0.04mm$^2$ on an unpatterned SH surface, which is a 4.7x reduction with a maximum of 8.5x. Therefore, particles in the droplet are highly concentrated due to evaporation on a SH surface.

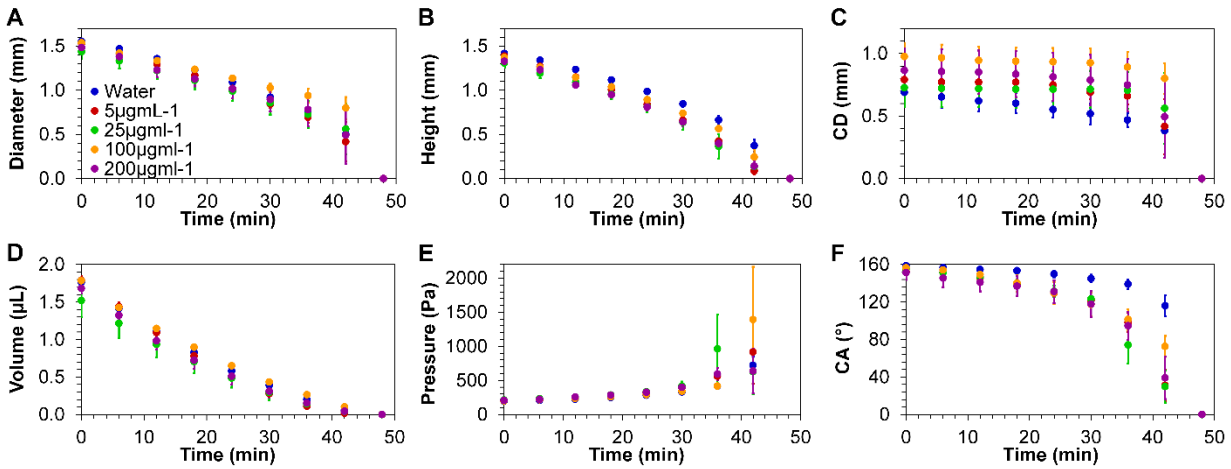


**Figure 5.6**: Characterization of 2µL of BSA suspended in water evaporating on a SH surface. A) Diameter, (B) Height, (C) Contact Diameter, (D) Volume, I Pressure, and (F) Contact Angle of BSA during evaporation. N=3

## 5.4 Protein Detection

### *5.4.1 Detection of BSA*

Evaporating BSA on a SH surface enhances detection compared to the standard, as shown in Figure 5.7. Droplets of 2µL, 10µL, and 20µL of BSA are confined to 500µm hydrophilic anchor points and during evaporation, the CD decreases 1.4x for 2µL and 2.5x for 10µL and 20µL, confining the contact area more than 5x for larger volumes. The anchor spots confine the evaporated droplet to a predictable footprint, ensure more even distribution of molecules in the final pellet, and allow high throughput detection using a patterned array (Figure 5.8). Evaporation on a SH surface yields a limit of detection (LOD) as low as 5µgmL$^{-1}$ for all tested volumes, and the detectable range is within 12.5-400µgmL$^{-1}$. The signal intensity is distinguishable for all BSA concentrations tested, and therefore, BSA concentration is quantifiable. Larger volumes have more pronounced signals with smaller error bars, allowing more precise diagnostics. Evaporation on a SH surface yields better signals compared to controls.

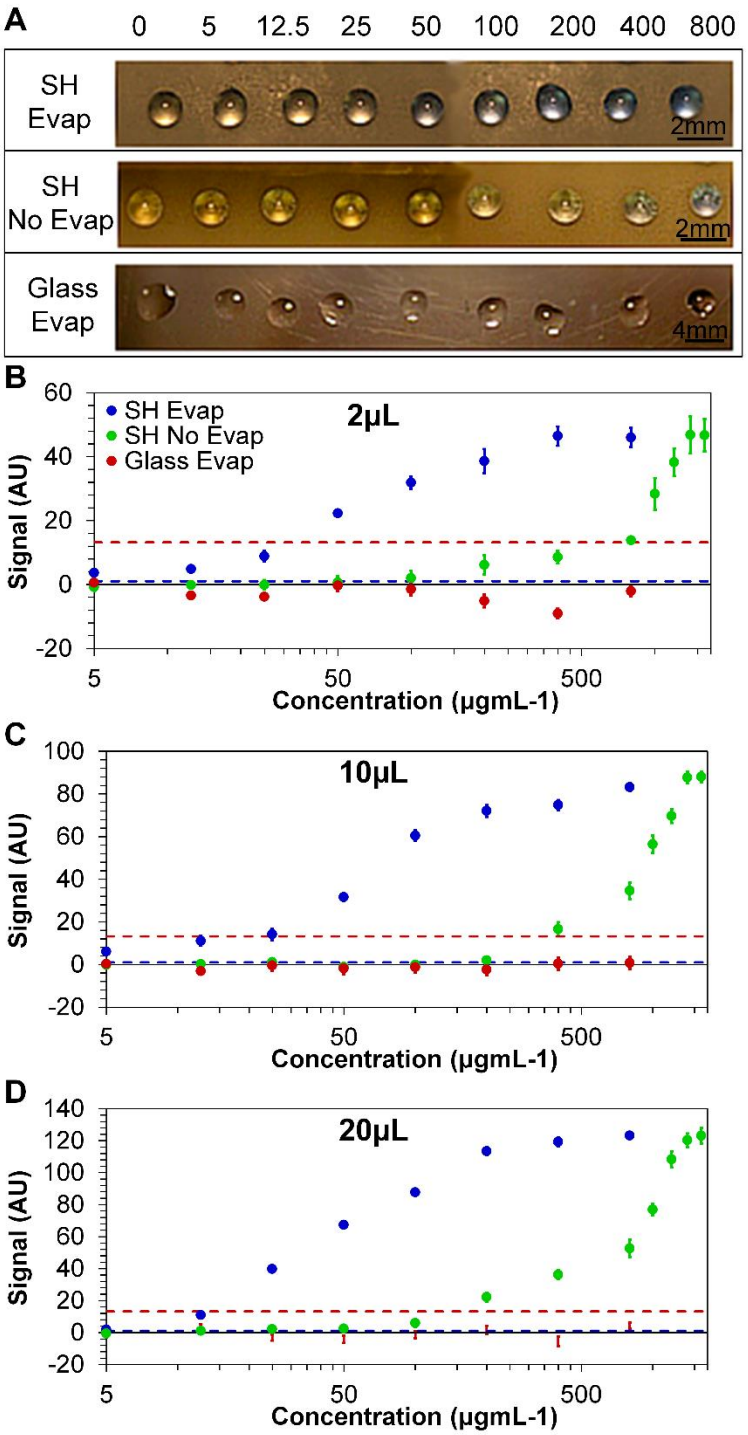


**Figure 5.7**: Evaporation on a SH surface improves protein detection, and BSA can be detected and distinguished between 12.5-400µgmL$^{1}$. (A) The colorimetric signal (due to the addition of detection dye) and drop shape are visualized on: a SH surface using evaporation, a SH surface without evaporation, and a glass surface with evaporation. The colorimetric signal is quantified with a (B) 2µL, (C) 10µL, and (D) 20µL droplet, and signal is highest for evaporation on a SH surface. Dashed blue lines represent the LOD signal for a SH surface, and dashed red lines represent the LOD signal for a glass surface. N=5

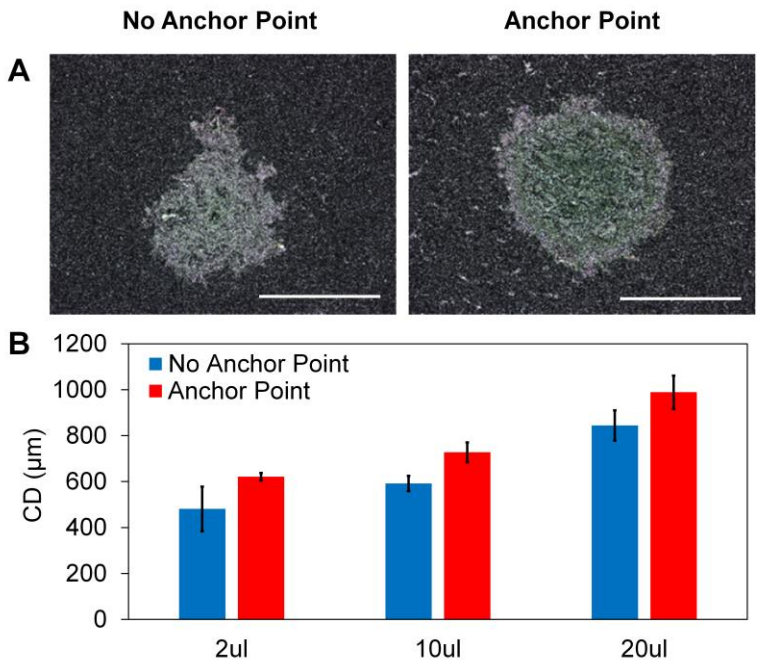


**Figure 5.8**: Hydrophilic anchor points allow consistent spot sizes, better distribution of molecules in the final pellet, and patterned arrays. A) Top down view of green food dye evaporated without and with anchor points. B) Contact diameter is larger with the anchor point, but molecules are more evenly distributed. Scale bars are 500µm.

As a control, the SH surface without evaporation has a detection range from 200-1500µgmL$^{-1}$. By comparing the detectable range with evaporation to the detectable range without evaporation on a superhydrophobic surface (Figure 5.9), the concentration effect due to evaporation is characterized (Figure 5.10), and evaporation on a SH surface yields 16x detection enhancement compared to without evaporation (in the linear detectable range). Molecules are also evaporated on the glass control, and the flat drop shape yields a low detection signal, leading to no BSA detection even at the highest concentrations tested. In addition, the inconsistent drop footprint on the glass surface leads to a higher background signal, preventing a detectable signal. Therefore, evaporation on a SH surface achieves greater than 160x enhancement compared to evaporation on glass.

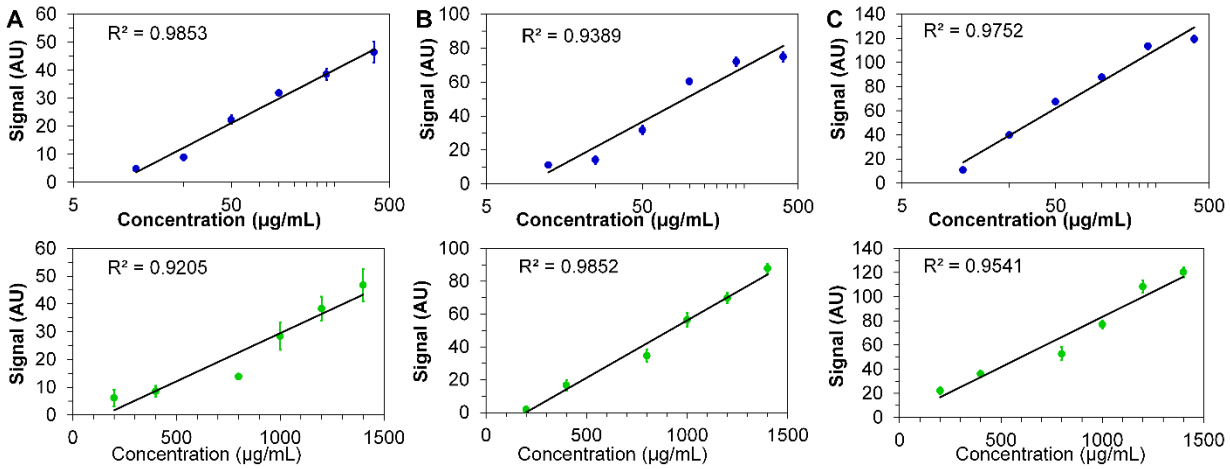


**Figure 5.9**: The linear regions of detection are used to determine the final concentration of BSA after evaporation. The signal of evaporated BSA (top) and signal of stock BSA is graphed for (A) 2µL, (B) 10µL, and (C) 20µL.

These results are significantly greater than the 5x enhancement achieved by McLauchlin et al. due to their detection reaction (protein crystallization) occurring during droplet evaporation. In the proposed design, the protein is completely evaporated before reacting with detection dye, and evaporation does not interfere with the detection reaction for signal enhancement. Also, detection dye has been evaporated on the SH surface, and BSA is added for protein detection. This resulting signal is comparable to evaporating BSA and adding detection dye (data not shown). By preloading detection dye for protein detection, the time to results can be decreased, making the device attractive for POC.

## 5.5 Pre-eclampsia Detection

### *5.4.1 Pre-eclampsia*

Pre-eclampsia effects 5-10% of pregnant women globally, and the diagnosis is critical to prevent seizures, stroke, organ failure, and even death to the mother and/or baby.[130–132] Symptoms of pre-eclampsia include weight gain, dizziness, swelling, nausea, and abdominal pain, but detection is concluded by a physical examination and a high level of protein in urine (more than 0.3g over a

24hour period). Urine must be collected over a long period of time and then sent to a trained technician for testing, making time to results more than one day. Therefore, a device sensitive enough to detect protein in urine from one sample would be beneficial. In one sample of urine, the average protein levels indicating pre-eclampsia range from 150-300µgmL$^{-1}$.

### *5.4.2 Enhanced Detection of Protein in Urine for Pre-eclampsia*

To test for pre-eclampsia, protein was spiked in urine samples from patients ranging from 0-310µgmL$^{-1}$ to analyze the normal and pre-eclampsia range of protein in urine (Figure 5.11). Normal protein levels (0-80µgmL$^{-1}$) are distinguishable from abnormal protein levels (150-300µgmL$^{-1}$) for all volumes tested. Horizontal error bars represent the variability of protein in urine from patient samples, and the level of protein in each sample is calculated based on the concentration curve from Figure 5.7. Also based on Figure 5.7, neither of the controls could detect the normal to pre-eclampsia range of protein.

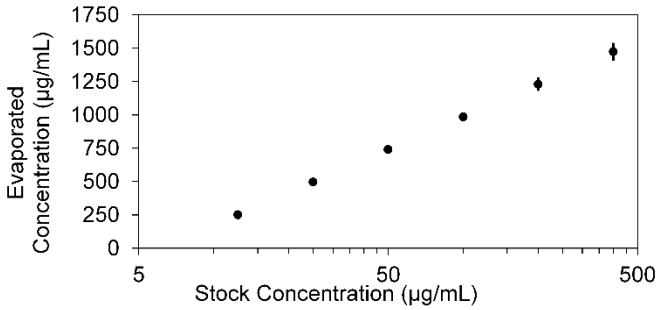


**Figure 5.10**: The stock concentration of BSA is plotted against the evaporated concentration of BSA, and the final concentration due to evaporation is determined.

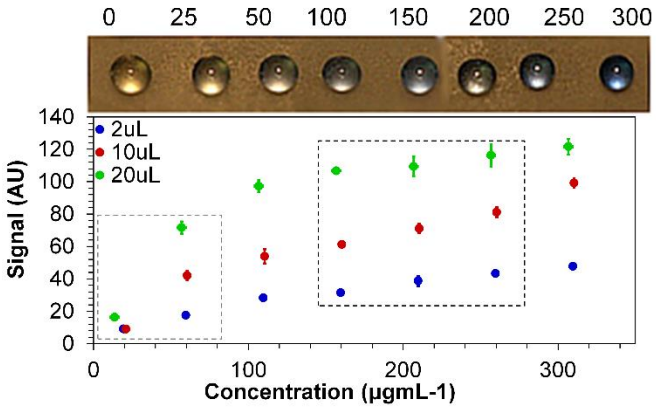


**Figure 5.11**: BSA spiked in urine is detectable and distinguishable using evaporation on a SH surface. Protein levels indicative of normal (dashed grey) to pre-eclampsia (dashed black) are shown. X-axis error bars represent the variability of protein in urine from patient samples. N=5

## 5.6 Summary

Evaporation on a SH surface concentrates molecules and reduces the contact area up to 8.5x. This concentrating effect leads to enhanced detection, and by evaporating on a SH surface, protein detection is 16x more sensitive than not evaporating (in the linear detectable range) and is greater than 160x more sensitive than the glass slide control. In addition, protein levels in urine are detectable and distinguishable to diagnose pre-eclampsia. This technique is simple to implement, is relatively fast (1-3hr), and does not require external processing or preparation. The colorimetric signal negates the need of expensive labeling and external equipment, as in fluorescence detection. Importantly, this simple method could also be readily integrated with more advanced detection techniques for improved detection. Finally, these SH surfaces are extremely simple and inexpensive to manufacture for true low-cost diagnostics.

# CHAPTER 6: Reduced Blood Coagulation on Superhydrophobic Surfaces

## 6.1 Blood Coagulation

Blood clotting poses significant challenges for medical devices and clinical applications. In medical applications, the blood coagulation cascade is initially triggered by the intrinsic pathway when blood is exposed to a foreign surface such as glass or plastic.[133,134] Upon exposure, the protein Factor XII on the surface of platelets is activated by binding to the charged surface, in turn activating thrombin conversion to fibrin.[134–136] Thrombin polymerizes fibrinogen to form the non-globular protein fibrin that acts as glue in a blood clot, and the amount of fibrin correlates with the progression of blood clotting.[134] Fibrin networks are formed when strands of fibrin cross-link, and fibrin networks act as scaffolds for cells (such as platelets and fibroblasts) and blood clotting factors.[137–139] Blood clotting is then amplified by the adherence of platelets to fibrin networks, and additional platelets are recruited to adhere, forming a hemostatic plug on a thrombogenic surface.[133,134,140] As fibrin networks form and platelets bind to fibrin, blood thickens and forms a blood clot within minutes.[141,142]

## 6.2 Blood Behavior on Superhydrophobic Surfaces

To prevent blood clotting in medical devices, anticoagulant drugs such as heparin and sodium citrate are pervasively used.[143–146] However, these drugs have drawbacks and may interfere with patient medication, medical procedures, or medical testing.[147–149] Alternatively, biomaterials have been used to prevent blood clotting by minimizing platelet adhesion and preventing the contact-activation pathway from being triggered.[133,150,151] SH surfaces have been shown to prevent the adhesion of protein and cells (i.e. more spherical and less spread out).[152–154] Further, SH surfaces have been shown to prevent platelet adhesion and therefore reduce blood coagulation.[143–146,150,151]

Sun *et al.* has shown a reduction in platelet adherence to their SH surface and has also shown that platelets adhered to SH surfaces are less mature than platelets adhered to flat surfaces.[150] Further, Leslie *et al.* has shown a reduced fibrin network as well as reduced thrombosis under flow *in vitro* and *in vivo* on their SH surfaces.[143] Both these systems show that SH surfaces reduce the activation of blood clotting. Of particular note, however, both systems use anticoagulants in their experiments and therefore have drawbacks to clinical applications. An ideal commercial device would obviate the use of anticoagulants altogether in order to be more compatible with clinical medicine.

### 6.3 Reduced Blood Adhesion to Superhydrophobic Surfaces

Figure 6.1 shows the behavior of blood on a SH surface compared to a flat surface. Multiple drops of blood are required for a droplet to slide off the 1”x3” flat strip (within 15 seconds), and visually, a significant amount of blood residue is smeared on the flat surface. Blood slides off the 1”x3” SH strip within 0.25 seconds and visually, no blood sticks to the SH surface. Visually, more blood adheres to the flat surface than the SH surface.

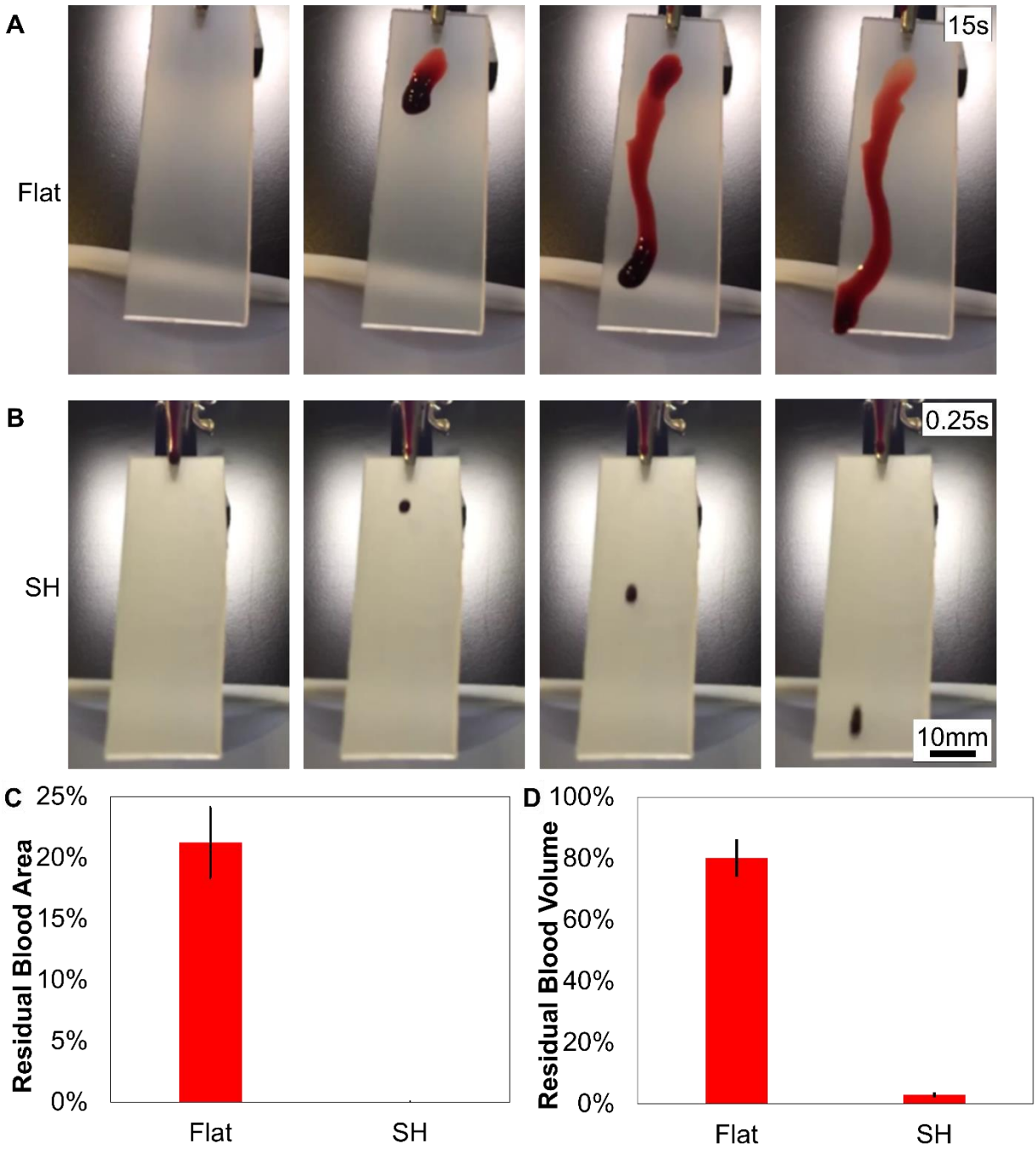


**Figure 6.1**: Still images of blood sliding on a flat and SH surface are taken with a high speed camera. A) Multiple drops of blood are required for blood to slide off the flat surface. Blood smears and partially slides off the flat surface within 15 seconds. B) One droplet of blood completely slides off the SH surface within 0.25 seconds and leaves no visual residue. Scale bar is 10mm for flat and SH. C) Blood residue area is reduced >4200x on the SH surface compared to flat. D) Significantly less blood volume adheres to the SH surface compared to flat (>28x).

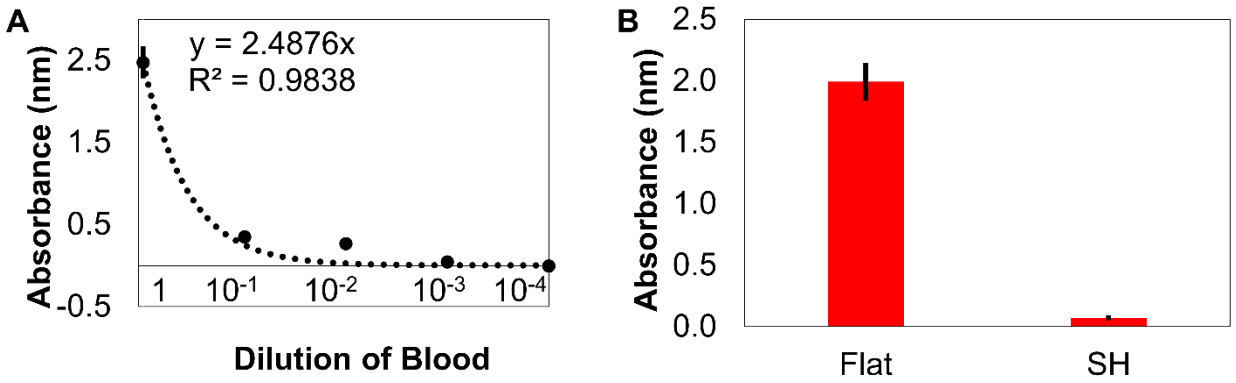


**Figure 6.2**: Blood volume residue is characterized by comparing absorbance values of a phenol-blood assay to a standard dilution curve. A) A standard curve for dilutions of blood in an absorbance plate reader (at 570nm). B) Absorbance values from blood residue were compared to absorbance values of blood dilutions to measure the amount of blood residue volume on flat and SH surfaces. Percent volume is calculated based on the standard curve.

Figure 6.1c-d measure the amount of blood residue area and volume adhered to a flat surface compared to a SH surface. The area of blood residue on the flat surface is 21 ± 5% and is within the noise for the SH surface (0.005 ± 0.004%), which is a more than 4200x reduction of blood area adherence. Blood residue volume on the SH and flat surfaces is measured using a phenol-blood assay. A standard dilution curve is created using dilutions of blood (Figure 6.2), and the absorbance values for blood residue volume are compared to the standard curve. 80 ± 15% of blood volume sticks to the flat surface compared to only 3 ± 2% of blood volume sticks to the SH surface, which is more than 28x reduction compared to flat and more than 35x reduction of overall blood volume adherence. [155]

### 6.4 Reduced Blood Coagulation on Superhydrophobic Surfaces

SH surfaces are shown to prevent blood coagulation using blood directly from the patient (i.e. without anticoagulants). Figure 6.3 shows the amount of fluorescently-labeled fibrin on the flat and SH surfaces, indicating the amount of blood clotting. Within the first 10min of incubation, the SH surfaces have significantly less blood clotting area compared to the flat surfaces, and the trend

continues for the 20 - 50min incubation times. Clotting area is reduced >170x for the initial 10min incubation time and is reduced >27x for the 20min and 30min incubation times. By the 40 – 50min incubation times, clotting is reduced 5x on the SH surfaces compared to flat. Blood coagulation is delayed on the SH surfaces due to the decrease in contact activation. Figure 6.3a pairs images of fluorescently-labeled fibrin with the data quantified in Figure 6.3b as the percent area of the fibrin clot.[143] Further, our SH surfaces use whole blood directly from the patient and negate the need for anticoagulants.

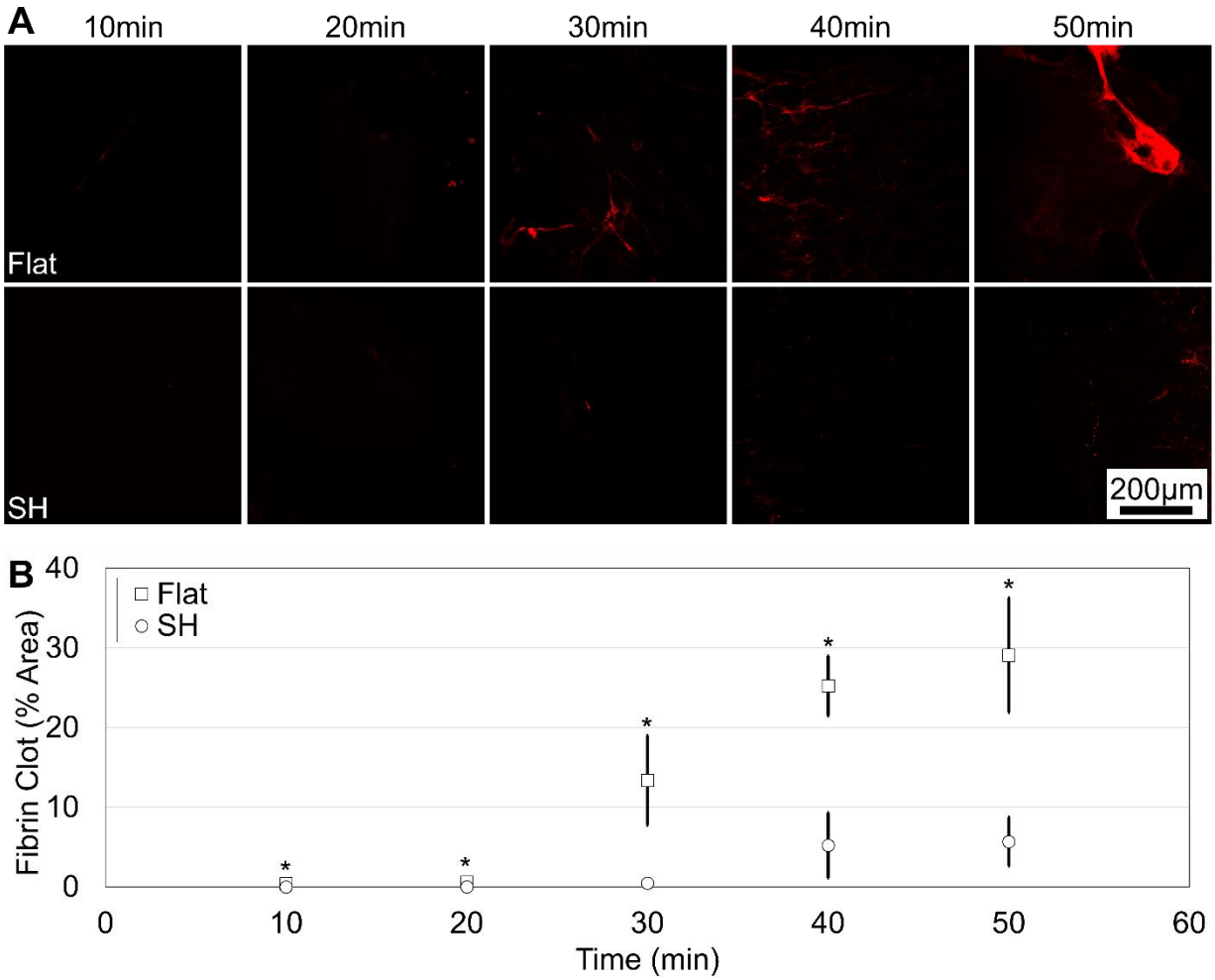


**Figure 6.3**: Blood coagulation is reduced on SH surfaces compared to flat. A) Fluorescently-labeled fibrinogen indicates blood coagulation on flat (top) and SH (bottom) surfaces. Scale bar is 200μm. B) SH surfaces have significantly less blood coagulation compared to flat (>5x reduction at 50min).

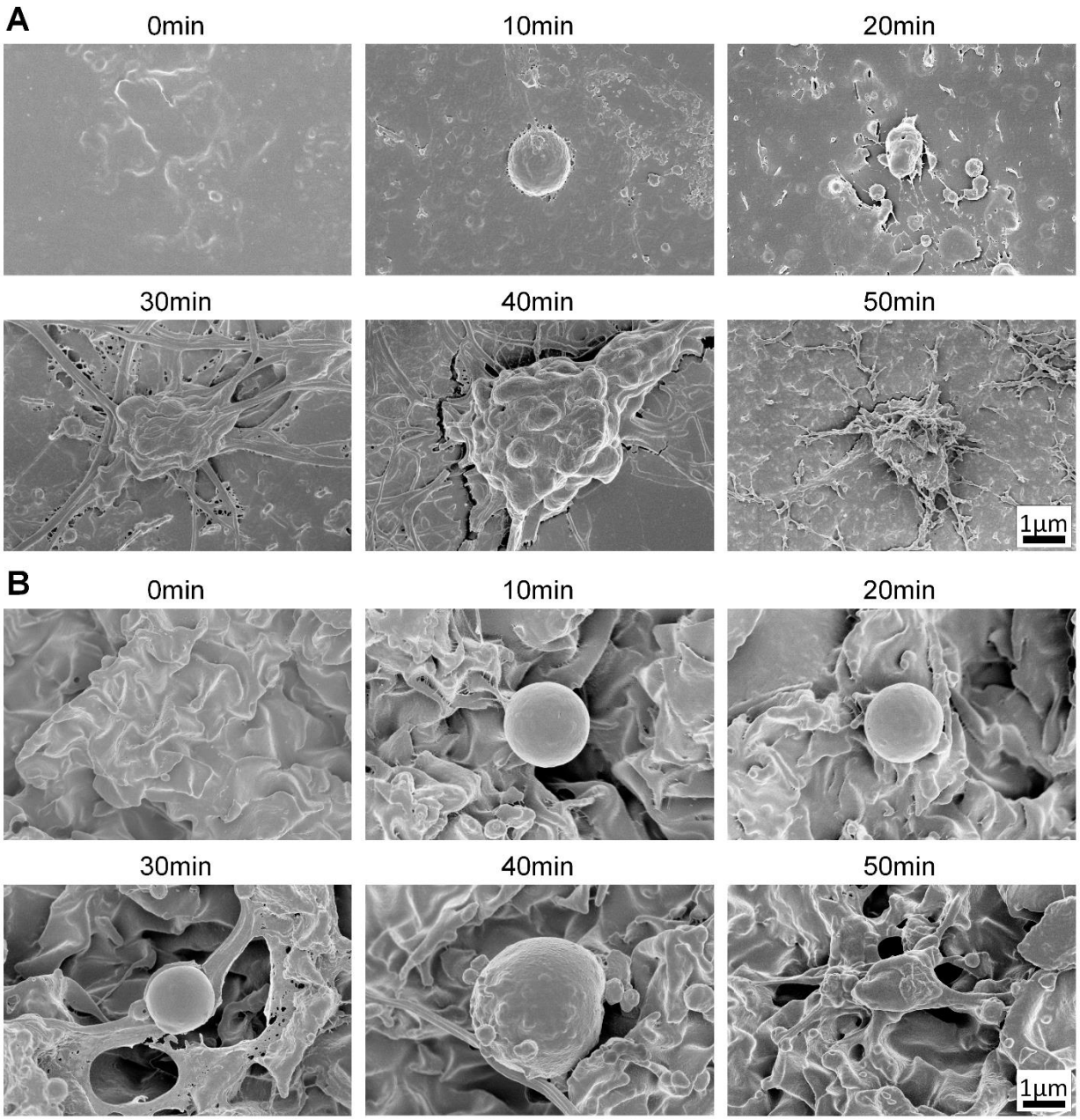


**Figure 6.4**: SEM images of blood coagulation on flat and SH surfaces for 0-50min time points. A) Flat surfaces show platelet maturation and fibrin formation within the first 20min of incubation. B) SH surfaces have less mature platelets up to 40min and fibrin formation is less prominent at the lower time points. Scale bars are 1µm for all images.

Figure 6.4 shows SEM images of the 10 - 50min blood coagulation incubation times as well as controls without blood coagulation for the flat and SH surfaces. Platelets begin to mature and fibrin networks begin to form by the 20min incubation time on the flat surfaces. By 30min, platelets are maturing and fibrin networks are forming. Platelets continue to mature, and fibrin networks

continue to grow at 30 – 50min incubation times on the flat surfaces. On the SH surface, however, platelets remain immature at the 40min incubation time and by 50min, platelets mature and spread along the peaks of the micro surfaces. Fibrin networks are seen at the 30min incubation time on SH surfaces and continue to form in the 40min and 50min incubation times. The fibrin networks form on the peaks of the micro structures, and platelets and fibrin span the micro valleys and attach to the micro peaks on the SH surfaces. Overall, SH surfaces have reduced fibrin network formation and platelet maturation on their surface compared to flat.[155]

### 6.5 Summary

Blood residue area is reduced >4200x, and blood residue volume is reduced >28x on the SH compared to flat. Blood coagulation is reduced >5x after 50min incubation, and platelet and fibrin network formation are less mature on a SH surface compared to the nonstructured flat counterpart. The anticoagulant nature of the SH surfaces negates the need for anticoagulant chemicals, broadening the potential medical applications of the SH surfaces. The proposed SH biomaterial is biocompatible and reduces blood coagulation. Therefore, the SH surfaces can function as an effective material for a plethora of medical applications.

# CHAPTER 7: Summary and Future Directions

## 7.1 Summary

In this dissertation, shrink-induced SH features have been translated from conception to application through scale-up manufacturing. By elegantly achieving hierarchical micro- to nanoscale features from commodity shrink film, purely structural SH features can be embossed into any commercially-available and FDA-approved plastics to achieve superhydrophobicity (Chapter 2). Making the fabrication process compatible with R2R manufacturing broadens the applications of SH technology and makes the technology readily-available for commercialization (Chapter 3).

Though there are infinite applications for SH technology, this dissertation has focused on antibacterial, enhanced POC detection, and anticoagulation. The SH plastics have been shown to prevent bacterial adhesion >150x more than a flat surface (Chapter 4). Detection in bodily fluids has been enhanced >160x for POC by simply evaporating fluid on the SH surface, and normal concentrations of protein in urine are distinguishable from pre-eclampsia concentrations of protein in urine (Chapter 5). Blood coagulation is reduced >5x on the SH surface using whole blood directly from the patients (Chapter 6).

This dissertation has demonstrated a few examples of SH applications, but there are still multiple applications to test. Thus, many more projects can be performed with the SH surfaces. Initial experiments include creating SH tubing and conformal shapes, generating the SH features directly in the shrink film, patterning the SH surfaces for additional detection assays using various bodily fluids, and implementing all the technology into a single fluidic detection device.

## 7.2 Future Directions

### *7.2.1 Rolled Superhydrophobic Tubing*

The R2R metalized masters are conformal during the shrinking process, and rolled SH tubes can created, as shown in Figure 7.1. SH features can be achieved on the inner and outer circumference of the tubes, and various diameters of tubes can be achieved for various applications. The SH features can be subsequently molded into polydimethylsiloxane (PDMS) to achieve SH rolled tubes of various diameters. Fluid slides through the flat and SH tubes (still images in Figure 7.1c and Figure 7.1d), and no residue remains on the SH tube, while fluid adheres to the flat tube. Due to the anticoagulant nature of the SH features and the conformability of the metalized PS master, the SH surfaces have potential for medical materials such as catheters, medical tubing, and microfluidic tubing. Such tubing could prevent blood clotting and tubing clogging for medical applications.

### *7.2.2 Argon Plasma Treated Superhydrophobic Shrink Film*

SH features can be achieved directly in the commodity PO shrink film by plasma treating with argon (Ar). Argon plasma treatment effectively etches the surface of the PO film and causes nanoscale roughness. Upon shrinking, the stiffness mismatch forms microscale wrinkle structures, and this hierarchy of features caused the substrate to become SH. SEM images in Figure 7.2 reveal the micro- to nanoscale features caused by Ar treatment. These substrates have CA >150˚ and CAH <10˚. FFT graphs reveal that Ar treated samples have features in the same SH regime as the initial SH samples and the R2R SH samples with the highest probability at ~1.2µm.

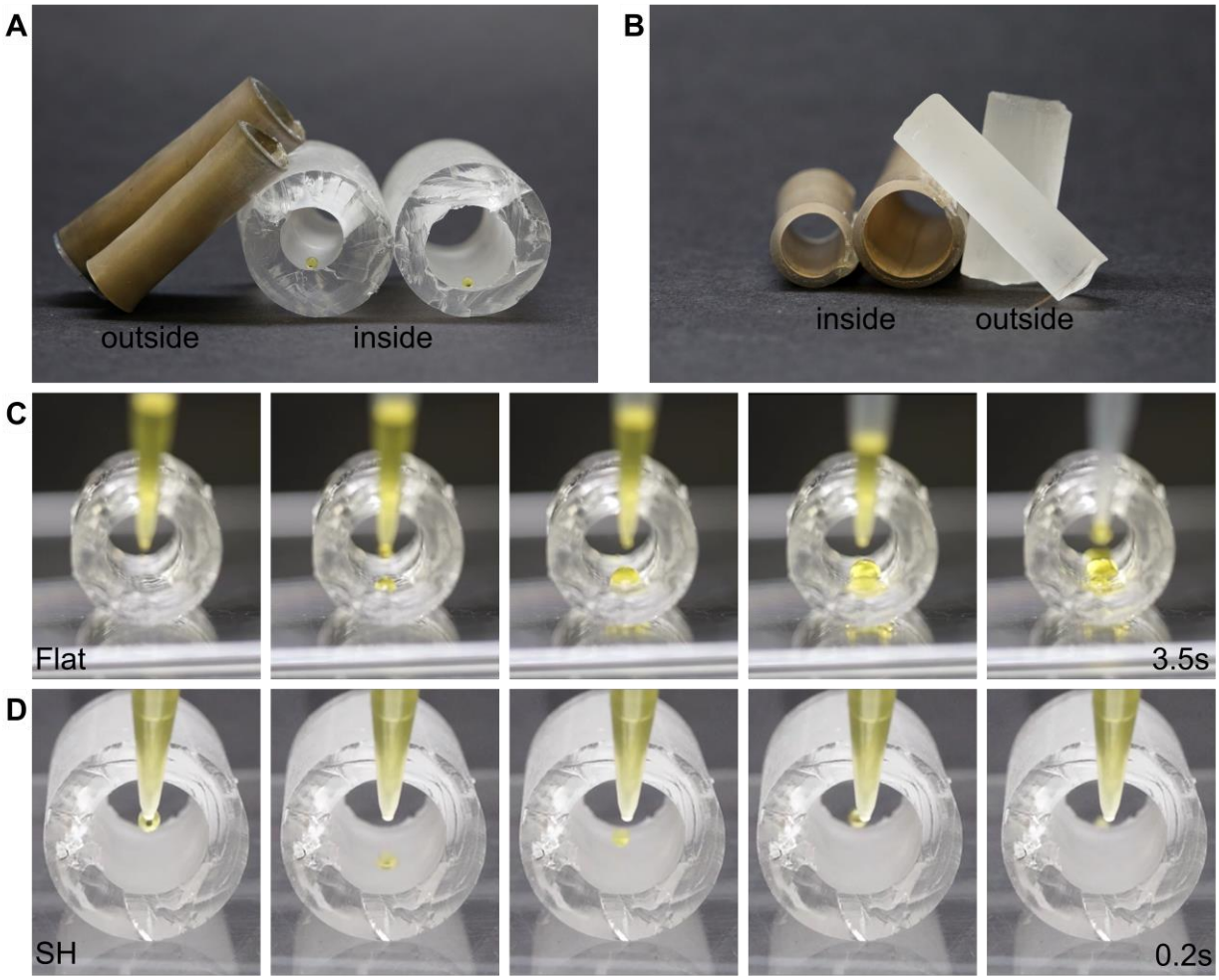


**Figure 7.1**: Metalized PS sheets are shrunk as rolled tubes with varying diameters. A) SH features are formed on the outside of the rolled PS, and when PDMS molds the features, SH PDMS tubes with features on the inside are created. Droplets of yellow food dye inside the tube have SH CA values. B) SH features are formed on the inside of the rolled PS, and when PDMS molds the features, SH cylinders with SH features on the outside are created. C) Still images of yellow food dye sliding in a flat tube. Multiple drops are needed for the droplet to slide off, and residue is left on the surface. D) Still images of yellow food dye sliding in a SH tube. Visually, no residue is left on the surface, and one droplet slides off within 0.2s.

Currently, substrate fabrication is limited by the argon chamber size as well as the time to treat the sample (more than 30min), which is dependent on the argon power. Argon plasma treatment is compatible with R2R manufacturing, and the argon power and time need to be optimized in a R2R platform to achieve mass production of SH features directly in the commodity shrink film.

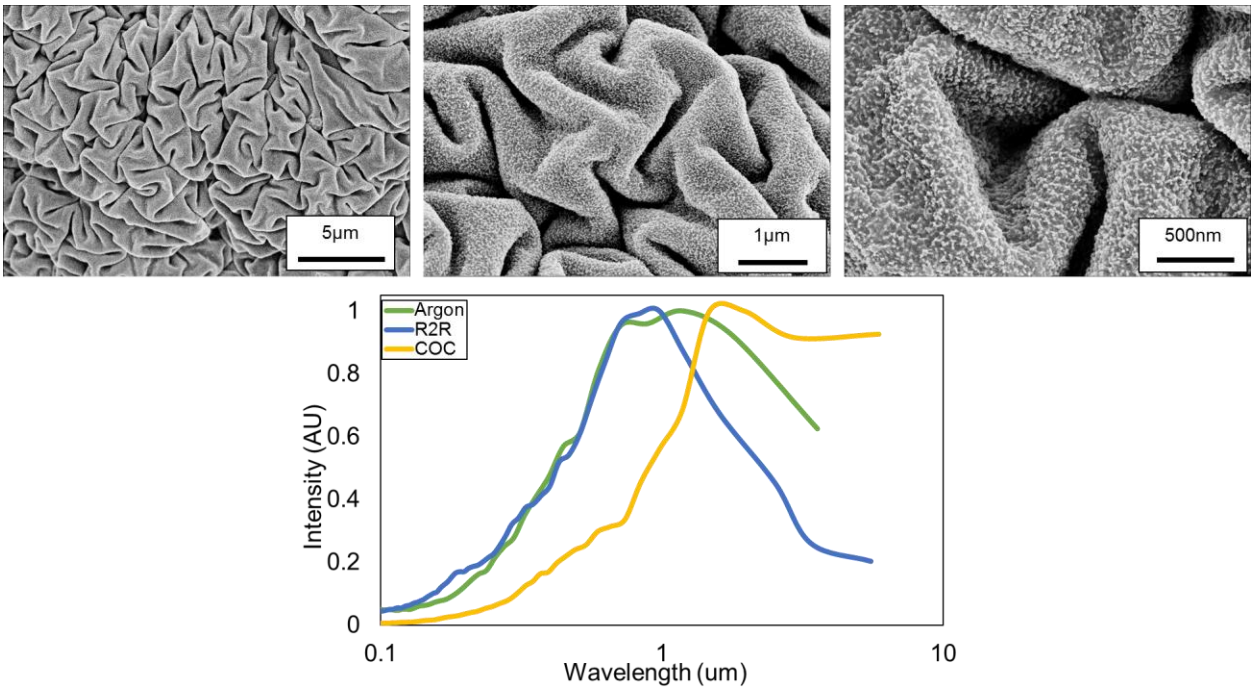


**Figure 7.2**: Shrink film is plasma treated with 60min of argon to achieve superhydrophobicity directly in the commodity shrink film. FFT graph shows the spatial frequency of argon treated samples with the R2R samples and initial fabrication protocol in embossed COC.

### *7.2.3 Patterned Detection on Superhydrophobic Shrink Substrates*

Previously, hydrophilic anchor points have been patterned on the SH surfaces by plasma treating through a negative mask (silica can also be deposited for longer hydrophilic effects compared to plasma). These hydrophilic anchor points can be achieved directly on the SH shrink film, and small volumes of fluids can be simply patterned on the SH surfaces. When fluid is deposited or rolled on the patterned SH surface, fluid preferentially sticks to the patterned anchor points and does not adhere to the SH regions. Therefore, fluid spatial deposition can be controlled. Enhanced concentration of protein in urine can be achieved by simply evaporating, and additional assays can also be performed.

**Figure 7.3**: Hydrophilic anchor points are created on the SH surface, and blood preferentially sticks to the hydrophilic regions. Due to the small volumes, colorimetric assays can be performed directly from whole blood.

Notably, assays can be performed directly from whole blood samples. Normally, the deep red color of blood hinders colorimetric assays, and blood must be diluted or pre-processed (such as centrifugation) to perform simple colorimetric assays. With the small volume capture method using the hydrophilic anchor points, colorimetric assays can be performed with whole blood, negating the need for processing, as shown in Figure 7.3.

Patterning the SH surfaces and capturing small volumes of blood will make the substrates compatible with complex bioassays that are often achieved using large volumes of separated blood in wells. The patterned SH substrate will require minimal reagents, and initial blood separations will be negated. Therefore, bioassays can be performed quickly without the need for large volumes of blood from patients.

### *7.2.4 Micro Superhydrophobic Ultra Rapid Flow (MicroSURF)*

Microfluidic devices are presently used for detection, but commercial adoption is hindered due to loss of reagents, sidewall adsorption, surface fouling, the need to drive flow, and interface issues. SH surfaces would elegantly address these issues to improve the state of microfluidic detection because of the unique physics of fluids on a SH surface.

The non-wetting behavior of the SH surfaces prevents loss of reagents and sidewall adsorption. In addition, the SH surfaces reduce fluid drag and have large slip lengths, approaching a “no-slip” condition. Therefore, instead of having a zero velocity at the channel wall (which results in the characteristic parabolic flow profile of pressure driven flow in microfluidic channels), flow on SH substrates slip on the surface. This results in a significantly lower pressure drop in microfluidic channels, minimizing the pressure needed to drive flow and also minimizing interface issues.

The need to detect very few molecules within a large dilute sample is a common challenge in biomedical microfluidic devices. A simple and elegant solution can be developed by integrating SH microfluidics with the enhanced detection in bodily fluids by simply evaporating large dilute volumes and detecting molecules in the concentrated solution. With this combination, previously complex biological assays can be easily performed.

# REFERENCES


[1] Office of the Federal Register National Archives and Records Administration, *Code of Federal Regulations, Title 21 - Food and Drugs*; 2015.

[2] J. F. Hecker, R. O. Edwards, *J. Biomed. Mater. Res.* **1981**, *15*, 1.

[3] R. I. Leininger, R. D. Falb, G. A. Grode, *Ann. New York Acad. Sci.* 11.

[4] K. Federov, C. Blaszyowski, S. Sheikh, A. Reheman, A. Romaschin, H. Ni, M. Thompson, *Langmuir* **2014**, 3217.

[5] G. F. Klein, H. Kofler, H. Wolf, P. O. Fritsch, *J. Am. Acad. Dermatol.* **1989**, *21*, 703.

[6] L. R. Freschauf, J. McLane, H. Sharma, M. Khine, Shrink-Induced Superhydrophobic and Antibacterial Surfaces in Consumer Plastics. *PLoS One* **2012**, *7*, 1.

[7] J. McLane, C. Wu, M. Khine, *Adv. Mater. Interfaces* **2015**, *2*, 1.

[8] B. D. Cassie, S. Baxter, *Trans. Faraday Soc.* **1944**, *40*, 546.

[9] R. N. Wenzel, *Ind. Eng. Chem.* **1936**, *28*, 988.

[10] H. Sharma, J. B. Wood, S. Lin, R. M. Corn, M. Khine, *Langmuir* **2014**, *30*, 10979.

[11] Y. T. Cheng, D. E. Rodak, C. a Wong, C. a Hayden, *Nanotechnology* **2006**, *17*, 1359.

[12] L. Feng, Y. Zhang, J. Xi, Y. Zhu, N. Wang, F. Xia, L. Jiang, *Langmuir* **2008**, *24*, 4114.

[13] Y. Zheng, X. Gao, L. Jiang, *Soft Matter* **2007**, *3*, 178.

[14] R. Helbig, J. Nickerl, C. Neinhuis, C. Werner, *PLoS One* **2011**, *6*, 2.

[15] L. Zhai, M. C. Berg, F. Ç. Cebeci, Y. Kim, J. M. Milwid, M. F. Rubner, R. E. Cohen, *Nano Lett.* **2006**, *6*, 1213.

[16] D. L. Hu, B. Chan, J. W. M. Bush, *Nature* **2003**, *424*, 663.

[17] F. Shi, J. Niu, J. Liu, F. Liu, Z. Wang, X. Q. Feng, X. Zhang, *Adv. Mater.* **2007**, *19*, 2257.

[18] G. S. Watson, B. W. Cribb, J. A. Watson, *PLoS One* **2011**, *6*.

[19] H. M. Whitney, R. Poetes, U. Steiner, L. Chittka, B. J. Glover, *PLoS One* **2011**, *6*, 1.

[20] M. Ma, R. M. Hill, *Curr. Opin. Colloid Interface Sci.* **2006**, *11*, 193.

[21] M. Nosonovsky, B. Bhushan, *Curr. Opin. Colloid Interface Sci.* **2009**, *14*, 270.

[22] A. Lafuma, D. Quéré, *Nat. Mater.* **2003**, *2*, 457.

[23] M. Ma, R. M. Hill, J. L. Lowery, S. V. Fridrikh, G. C. Rutledge, *Langmuir* **2005**, *21*, 5549.

[24] G. McHale, N. J. Shirtcliffe, M. I. Newton, *Langmuir* **2004**, *20*, 10146.

[25] Q. F. Xu, J. N. Wang, K. D. Sanderson, *Am. Chem. Soc. Nano* **2010**, *4*, 2201.

[26] H. Y. Erbil, a L. Demirel, Y. Avci, O. Mert, *Sci. Reports* **2003**, *299*, 1377.

[27] G. Blanco-Gomez, L. M. Flendrig, J. M. Cooper, *Langmuir* **2010**, *26*, 7248.

[28] D. Öner, T. J. McCarthy, *Langmuir* **2000**, *16*, 7777.

[29] V. Jokinen, L. Sainiemi, S. Franssila, *Adv. Mater.* **2008**, *20*, 3453.

[30] S. S. Guo, M. H. Sun, J. Shi, Y. J. Liu, W. H. Huang, C. Combellas, Y. Chen, *Microelectron. Eng.* **2007**, *84*, 1673.

[31] B. Cortese, S. D. Amone, M. Manca, I. Viola, R. Cingolani, G. Gigli, *Langmuir* **2008**, 2712.

[32] J. Genzer, K. Efimenko, *Sci. Reports* **2000**, *290*, 2130.

[33] B. J. Privett, J. Youn, S. a Hong, J. Lee, J. Han, J. H. Shin, M. H. Schoenfisch, *Langmuir* **2011**, *27*, 9597.

[34] J. Wu, J. Xia, W. Lei, B. Wang, *PLoS One* **2010**, *5*.

[35] X. Lu, C. Zhang, Y. Han, *Macromol. Rapid Commun.* **2004**, *25*, 1606.

[36] J.-Y. Shiu, C.-W. Kuo, P. Chen, *Proc. SPIE* **2004**, *5648*, 325.

[37] T. Young, *Philos. Trans. R. Soc. London* **1805**, *95*, 65.

[38] D. B. Abraham, L. F. Ko, *Phys. Rev. Lett.* **1989**, *63*, 275.

[39] A. Nakajima, *NPG Asia Mater.* **2011**, *3*, 49.

[40] S. Yang, K. Khare, P. C. Lin, *Adv. Funct. Mater.* **2010**, *20*, 2550.

[41] J. Y. Chung, A. J. Nolte, C. M. Stafford, *Adv. Mater.* **2011**, *23*, 349.

[42] C.-C. Fu, A. Grimes, M. Long, C. G. L. Ferri, B. D. Rich, S. Ghosh, S. Ghosh, L. P. Lee, A. Gopinathan, M. Khine, *Adv. Mater.* **2009**, *21*, 4472.

[43] C.-C. Fu, G. Ossato, M. Long, M. a. Digman, A. Gopinathan, L. P. Lee, E. Gratton, M. Khine, *Appl. Phys. Lett.* **2010**, *97*, 203101.

[44] U. Manna, M. C. D. Carter, D. M. Lynn, *Adv. Mater.* **2013**, *25*, 3085.

[45] Y. Rahmawan, M. W. Moon, K. S. Kim, K. R. Lee, K. Y. Suh, *Langmuir* **2010**, *26*, 484.

[46] J. H. Lee, H. W. Ro, R. Huang, P. Lemaillet, T. a. Germer, C. L. Soles, C. M. Stafford, *Nano Lett.* **2012**, *12*, 5995.

[47] C.-S. Chen, D. N. Breslauer, J. I. Luna, A. Grimes, W.-C. Chin, L. P. Lee, M. Khine, *Lab Chip* **2008**, *8*, 622.

[48] D. Nguyen, D. Taylor, K. Qian, N. Norouzi, J. Rasmussen, S. Botzet, M. Lehmann, K. Halverson, M. Khine, *Lab Chip* **2010**, *10*, 1623.

[49] A. Grimes, D. N. Breslauer, M. Long, J. Pegan, L. P. Lee, M. Khine, *Lab Chip* **2008**, *8*, 170.

[50] D. Taylor, D. Dyer, V. Lew, M. Khine, *Lab Chip* **2010**, *10*, 2472.

[51] M. Long, M. a. Sprague, A. a. Grimes, B. D. Rich, M. Khine, *Appl. Phys. Lett.* **2009**, *94*, 25.

[52] D. Nguyen, J. McLane, V. Lew, J. Pegan, M. Khine, *Biomicrofluidics* **2011**, *5*, 22209.

[53] D. Nawarathna, N. Norouzi, J. McLane, H. Sharma, N. Sharac, T. Grant, A. Chen, S. Strayer, R. Ragan, M. Khine, *Appl. Phys. Lett.* **2013**, *102*, 63504.

[54] D. Nguyen, S. Sa, J. D. Pegan, B. Rich, G. Xiang, K. E. McCloskey, J. O. Manilay, M. Khine, *Lab Chip* **2009**, *9*, 3338.

[55] J. I. Luna, J. Ciriza, M. E. Garcia-Ojeda, M. Kong, A. Herren, D. K. Lieu, R. a Li, C. C. Fowlkes, M. Khine, K. E. McCloskey, *Tissue Eng. Part C. Methods* **2011**, *17*, 579.

[56] V. Lew, D. Nguyen, M. Khine, *J. Lab. Autom.* **2011**, *16*, 450.

[57] A. Chen, D. K. Lieu, L. Freschauf, V. Lew, H. Sharma, J. Wang, D. Nguyen, I. Karakikes, R. J. Hajjar, A. Gopinathan, E. Botvinick, C. C. Fowlkes, R. a. Li, M. Khine, *Adv. Mater.* **2011**, *23*, 5785.

[58] J. Wang, A. Chen, D. K. Lieu, I. Karakikes, G. Chen, W. Keung, C. W. Chan, R. J. Hajjar, K. D. Costa, M. Khine, R. a. Li, *Biomaterials* **2013**, *34*, 8878.

[59] D. Dyer, S. Shreim, S. Jayadev, V. Lew, E. Botvinick, M. Khine, *Appl. Phys. Lett.* **2011**, *99*, 99.

[60] M. Long, M. Khine, A. D. KIm, *J. Opt. Soc. Am. A* **2010**, *27*, 1002.

[61] S. Jayadev, J. Pegan, D. Dyer, J. McLane, J. Lim, M. Khine, *Smart Mater. Struct.* **2013**, *22*, 014014.

[62] C. G. L. Ferri, R. H. Inman, B. Rich, A. Gopinathan, M. Khine, S. Ghosh, *Opt. Mater. Express* **2013**, *3*, 383.

[63] S. Lin, H. Sharma, M. Khine, *Adv. Opt. Mater.* **2013**.

[64] H. Sharma, M. a. Digman, N. Felsinger, E. Gratton, M. Khine, *Opt. Mater. Express* **2014**, *4*, 753.

[65] S. Lin, E. K. Lee, M. Khine, *Lab Chip* **2014**, *14*, 3475.

[66] J. D. Pegan, A. Y. Ho, M. Bachman, M. Khine, *Lab Chip* **2013**, *13*, 4205.

[67] X.-M. Zhao, Y. Xia, G. M. Whitesides, *J. Mater. Chem.* **1997**, *7*, 1069.

[68] Y. Xia, G. M. Whitesides, *Annu. Rev. Mater. Sci.* **1998**, *28*, 153.

[69] J. R. Anderson, D. T. Chiu, R. J. Jackman, O. Chemiavskaya, J. C. McDonald, H. Wu, S. H. Whitesides, G. M. Whitesides, *Anal. Chem.* **2000**, *72*, 3158.

[70] G. M. Whitesides, E. Ostuni, X. Jiang, D. E. Ingber, *Annu. Rev. Biomed. Eng.* **2001**, *3*, 335.

[71] H. Chen, M. a. Brook, H. Sheardown, *Biomaterials* **2004**, *25*, 2273.

[72] B. V. Bartzoka, M. R. Mcdermott, M. a Brook, *Adv. Mater. Mater* **1999**, *11*, 257.

[73] D. J. Beebe, G. a Mensing, G. M. Walker, *Annu. Rev. Biomed. Eng.* **2002**, *4*, 261.

[74] H. Becker, U. Heim, *Sensors Actuators, A Phys.* **2000**, *83*, 130.

[75] V. N. Goral, Y.-C. Hsieh, O. N. Petzold, R. a Faris, P. K. Yuen, *J. Micromechanics Microengineering* **2011**, *21*, 017002.

[76] J. Steigert, S. Haeberle, T. Brenner, C. Müller, C. P. Steinert, P. Koltay, N. Gottschlich, H. Reinecke, J. Rühe, R. Zengerle, J. Ducrée, *J. Micromechanics Microengineering* **2007**, *17*, 333.

[77] J. Li, D. Chen, G. Chen, *Anal. Lett.* **2005**, *38*, 1127.

[78] T. D. Boone, Z. H. Fan, H. H. Hooper, A. J. Ricco, H. Tan, J. Stephen, *Anal. Chem.* **2002**, 78.

[79] M. D. Huntington, J. Engel, A. J. Hryn, T. W. Odom, *Appl. Mater. Interfaces* **2013**, *5*, 6438.

[80] A. F. Stalder, T. Melchior, M. Müller, D. Sage, T. Blu, M. Unser, *Colloids Surfaces A Physicochem. Eng. Asp.* **2010**, *364*, 72.

[81] L. Zhu, Y. Xiu, J. Xu, P. a Tamirisa, D. W. Hess, C.-P. Wong, *Langmuir* **2005**, *21*, 11208.

[82] B. Bhushan, Y. C. Jung, *Prog. Mater. Sci.* **2011**, *56*, 1.

[83] M. Liu, S. Wang, Z. Wei, Y. Song, L. Jiang, *Adv. Mater.* **2009**, *21*, 665.

[84] Z. Chu, S. Seeger, *Chem. Soc. Rev.* **2014**, *43*, 2784.

[85] B. Qian, Z. Shen, *Langmuir* **2005**, *21*, 9007.

[86] R. Fürstner, W. Barthlott, C. Neinhuis, P. Walzel, *Langmuir* **2005**, *21*, 956.

[87] N. J. Shirtcliffe, G. McHale, M. I. Newton, C. C. Perry, *Langmuir* **2003**, *19*, 5626.

[88] T. Baldacchini, J. E. Carey, M. Zhou, E. Mazur, *Langmuir* **2006**, *22*, 4917.

[89] X. Feng, L. Feng, M. Jin, J. Zhai, L. Jiang, D. Zhu, *J. Am. Chem. Soc.* **2004**, *126*, 62.

[90] Kobrin, Rolith, Nanostructures with Anti-Counterfeiting Features and Methods of Fabricating the Same **2011**.

[91] J. D. Smith, LiqiGlide, Non-Toxis Liquid Impregnated Surfaces. *Can. Med. Assoc. J.* **2015**.

[92] R. Liedert, L. K. Amundsen, A. Hokkanen, M. Mäki, A. Aittakorpi, M. Pakanen, J. R. Scherer, R. a. Mathies, M. Kurkinen, S. Uusitalo, L. Hakalahti, T. K. Nevanen, H. Siitari, H. Söderlund, *Lab Chip* **2012**, *12*, 333.

[93] *Roll to Roll (R2R) Processing Technology Assessment*.

[94] L. Peng, Y. Deng, P. Yi, X. Lai, *J. Micromechanics Microengineering* **2014**, *24*, 013001.

[95] V. N. Kazakov, A. A. Udod, I. I. Zinkovych, V. B. Fainerman, R. Miller, *Colloids Surfaces B Biointerfaces* **2009**, *74*, 457.

[96] R. D. Scott, *Cdc* **2009**, 13.

[97] A. Gaidelyté, M. Vaara, D. H. Bamford, *PLoS One* **2007**, *2*, 1.

[98] R. M. Klevens, J. R. Edwards, C. L. Richards, T. C. Horan, R. P. Gaynes, D. a. Pollock, D. M. Cardo, *Public Health Rep.* **2007**, *122*, 160.

[99] G. E. Flores, S. T. Bates, D. Knights, C. L. Lauber, J. Stombaugh, R. Knight, N. Fierer, *PLoS One* **2011**, *6*.

[100] J. S. Brooke, J. W. Annand, A. Hammer, K. Dembkowski, S. T. Shulman, *J. Environ. Health* **2009**.

[101] P. Srikanth, E. Rajaram, S. Sudharsanam, a. Lakshmanan, U. S. S. Mariappan, K. Jagannathan, *J. Infect. Prev.* **2010**, *11*, 87.

[102] I. Sondi, B. Salopek-Sondi, *J. Colloid Interface Sci.* **2004**, *275*, 177.

[103] K. H. Cho, J. E. Park, T. Osaka, S. G. Park, *Electrochim. Acta* **2005**, *51*, 956.

[104] S. Hou, E. a. Burton, K. a. Simon, D. Blodgett, Y. Y. Luk, D. Ren, *Appl. Environ. Microbiol.* **2007**, *73*, 4300.

[105] L. Y. Zheng, J. F. Zhu, *Carbohydr. Polym.* **2003**, *54*, 527.

[106] D. I. Andersson, D. Hughes, *Nat. Rev. Microbiol.* **2010**, *8*, 260.

[107] N. J. Hallab, K. J. Bundy, K. O'Connor, R. L. Moses, J. J. Jacobs, *Tissue Eng.* **2001**, *7*, 55.

[108] H. Yang, Y. Deng, *J. Colloid Interface Sci.* **2008**, *325*, 588.

[109] J. H. Pringle, M. Fletcher, *Appl. Environ. Microbiol.* **1986**, *51*, 1321.

[110] R. Bhattacharya, C. R. Patra, S. Wang, L. Lu, M. J. Yaszemski, D. Mukhopadhyay, P. Mukherjee, *Adv. Funct. Mater.* **2006**, *16*, 395.

[111] M. T. Hurley, Z. Wang, A. Mahle, D. Rabin, Q. Liu, D. S. English, M. R. Zachariah, D. Stein, P. DeShong, *Adv. Funct. Mater.* **2013**, *23*, 3335.

[112] Y.-C. Liu, C.-K. Chiang, H.-T. Chang, Y.-F. Lee, C.-C. Huang, *Adv. Funct. Mater.* **2011**, *21*, 4448.

[113] H.-S. Seo, S.-E. Kim, J.-S. Park, J.-H. Lee, K.-Y. Yang, H. Lee, K. E. Lee, S.-S. Han, J. Lee, *Adv. Funct. Mater.* **2010**, *20*, 4055.

[114] Y. Zhao, X. Zhao, Z. Gu, *Adv. Funct. Mater.* **2010**, *20*, 2970.

[115] W. Hu, Y. Liu, Z. Lu, C. M. Li, *Adv. Funct. Mater.* **2010**, *20*, 3497.

[116] P. J. Yunker, T. Still, M. a Lohr, a G. Yodh, *Nature* **2011**, *476*, 308.

[117] T. S. Wong, T. H. Chen, X. Shen, C. M. Ho, *Anal. Chem.* **2011**, *83*, 1871.

[118] G. McHale, S. Aqil, N. J. Shirtcliffe, M. I. Newton, H. Y. Erbil, *Langmuir* **2005**, *21*, 11053.

[119] C.-H. Choi, C.-J. C. J. Kim, *Langmuir* **2009**, *25*, 7561.

[120] M. L. McLauchlin, D. Yang, P. Aella, A. A. Garcia, S. T. Picraux, M. A. Hayes, *Langmuir* **2007**, *23*, 4871.

[121] R. Seemann, M. Brinkmann, E. J. Kramer, F. F. Lange, R. Lipowsky, *Proc. Natl. Acad. Sci. U. S. A.* **2005**, *102*, 1848.

[122] K. Khare, J. Zhou, S. Yang, *Langmuir* **2009**, *25*, 12794.

[123] E. Bormashenko, R. Pogreb, G. Whyman, M. Erlich, *Langmuir* **2007**, *23*, 6501.

[124] E. Bormashenko, R. Pogreb, G. Whyman, M. Erlich, *Langmuir* **2007**, *23*, 12217.

[125] F. De Angelis, F. Gentile, F. Mecarini, G. Das, M. Moretti, P. Candeloro, M. L. Coluccio, G. Cojoc, A. Accardo, C. Liberale, R. P. Zaccaria, G. Perozziello, L. Tirinato, A. Toma, G. Cuda, R. Cingolani, E. Di Fabrizio, *Nat. Photonics* **2011**, *5*, 682.

[126] W. Li, A. Amirfazli, *J. Colloid Interface Sci.* **2005**, *292*, 195.

[127] X. Zhang, S. Tan, N. Zhao, X. Guo, X. Zhang, Y. Zhang, J. Xu, *Chemphyschem* **2006**, *7*, 2067.

[128] Y. C. Jung, B. Bhushan, *J. Microsc.* **2008**, *229*, 127.

[129] F. Gentile, M. L. Coluccio, N. Coppedè, F. Mecarini, G. Das, C. Liberale, L. Tirinato, M. Leoncini, G. Perozziello, P. Candeloro, F. De Angelis, E. Di Fabrizio, *ACS Appl. Mater. Interfaces* **2012**, *4*, 3213.

[130] B. Sibai, G. Dekker, M. Kupferminc, A. S. Way, *Lancet* **2005**, *365*, 785.

[131] J. M. Roberts, D. W. Cooper, *Lancet* **2001**, *357*, 53.

[132] L. C. Kenny, W. B. Dunn, D. I. Ellis, J. Myers, P. N. Baker, D. B. Kell, *Metabolomics* **2005**, *1*, 227.

[133] N. Mackman, R. E. Tilley, N. S. Key, *Arterioscler. Thromb. Vasc. Biol.* **2007**, *27*, 1687.

[134] B. Furie, B. C. Furie, *Cell* **1988**, *53*, 505.

[135] D. E. Cool, R. T. a Macgillivray, **1987**, *262*, 13662.

[136] E. Stavrou, A. H. Schmaier, *Thromb. Res.* **2010**, *125*, 210.

[137] R. A. Campbell, K. A. Overmyer, C. H. Selzman, B. C. Sheridan, A. S. Wolberg, *Blood* **2009**, *114*, 4886.

[138] J. P. Collet, D. Park, C. Lesty, J. Soria, C. Soria, G. Montalescot, J. W. Weisel, *Arterioscler. Thromb. Vasc. Biol.* **2000**, *20*, 1354.

[139] I. N. Chernysh, J. W. Weisel, W. Dc, *Network* **2011**, *111*, 4854.

[140] J. W. M. Heemskerk, E. M. Bevers, T. Lindhout, *Thromb. Haemost.* **2002**, *88*, 186.

[141] J. F. Mustard, M. A. Packham, *Br. Med. Bull.* **1977**, *33*, 187.

[142] V. Pešáková, D. Kubies, H. Hulejová, L. Himmlová, *J. Mater. Sci. Mater. Med.* **2007**, *18*, 465.

[143] D. C. Leslie, A. Waterhouse, J. B. Berthet, T. M. Valentin, A. L. Watters, A. Jain, P. Kim, B. D. Hatton, A. Nedder, K. Mullen, E. H. Super, C. Howell, C. P. Johnson, T. L. Vu, S. Rifai, A. Hansen, M. Aizenberg, M. Super, J. Aizenberg, D. E. Ingber, *Nat. Biotechnol.* **2014**, *32*, 1134.

[144] Z. Zhang, J. Borenstein, L. Guiney, R. Miller, S. Sukavaneshvar, C. Loose, *Lab Chip* **2013**, *13*, 1963.

[145] X. Hou, X. Wang, Q. Zhu, J. Bao, C. Mao, L. Jiang, J. Shen, *Colloids Surfaces B Biointerfaces* **2010**, *80*, 247.

[146] C. Mao, C. Liang, W. Luo, J. Bao, J. Shen, X. Hou, W. Zhao, *J. Mater. Chem.* **2009**, *19*, 9025.

[147] A. Power, N. Duncan, S. K. Singh, W. Brown, E. Dalby, C. Edwards, K. Lynch, V. Prout, T. Cairns, M. Griffith, A. McLean, A. Palmer, D. Taube, *Am. J. Kidney Dis.* **2009**, *53*, 1034.

[148] R. Renzi, S. Finkbeiner, *Am. J. Emerg. Med.* **1991**, *9*, 551.

[149] J. M. Walenga, R. L. Bick, *Curr. Concept Thromb.* **1998**, *82*, 635.

[150] T. Sun, H. Tan, D. Han, Q. Fu, L. Jiang, *Small* **2005**, *1*, 959.

[151] M. Zhou, J. H. Yang, X. Ye, A. R. Zheng, G. Li, P. F. Yang, Y. Zhu, L. Cai, *J. Nano Res.* **2008**, *2*, 129.

[152] Y. Koc, a J. de Mello, G. McHale, M. I. Newton, P. Roach, N. J. Shirtcliffe, *Lab Chip* **2008**, *8*, 582.

[153] N. M. Alves, J. Shi, E. Oramas, J. L. Santos, H. Tomás, J. F. Mano, *J. Biomed. Mater. Res. - Part A* **2009**, *91*, 480.

[154] E. Luong-Van, I. Rodriguez, H. Y. Low, N. Elmouelhi, B. Lowenhaupt, S. Natarajan, C. T. Lim, R. Prajapati, M. Vyakarnam, K. Cooper, *J. Mater. Res.* **2012**, *28*, 165.

[155] J. M. Nokes, R. Liedert, M. Kim, A. Siddiqui, M. Chu, E. Lee, M. Khine, *Reduced Blood Coagulation on Roll-to-Roll, Shrink-Induced Superhydrophobic Plastics*; 2015.